Donald M. Evans, Vincent Garcia, Dennis Meier and Manuel Bibes

11 Domains and domain walls in multiferroics

Abstract: Multiferroics are materials combining several ferroic orders, such as ferroelectricity, ferro- (or antiferro-) magnetism, ferroelasticity and ferrotoroidicity. They are of interest both from a fundamental perspective, as they have multiple (coupled) non-linear functional responses providing a veritable myriad of correlated phenomena, and because of the opportunity to apply these functionalities for new device applications. One application is, for instance, in non-volatile memory, which has led to special attention being devoted to ferroelectric and magnetic multiferroics. The vision is to combine the low writing power of ferroelectric information with the easy, non-volatile reading of magnetic information to give a "best of both worlds" computer memory. For this to be realised, the two ferroic orders need to be intimately linked via the magnetoelectric effect. The magnetoelectric coupling – the way polarization and magnetization interact – is manifested by the formation and interactions of domains and domain walls, and so to understand how to engineer future devices one must first understand the interactions of domains and domain walls. In this article, we provide a short introduction to the domain formation in ferroelectrics and ferromagnets, as well as different microscopy techniques that enable the visualization of such domains. We then review the recent research on multiferroic domains and domain walls, including their manipulation and intriguing properties, such as enhanced conductivity and anomalous magnetic order. Finally, we discuss future perspectives concerning the field of multiferroic domain walls and emergent topological structures such as ferroelectric vortices and skyrmions.

Keywords: multiferroic, domains, domain walls, microscopy

11.1 Domain structures in (multi-)ferroics

11.1.1 Introduction to ferroic domains and domain walls

Ferroic materials are defined by the appearance of an order parameter (e.g., elastic, electric or magnetic) at a non-disruptive phase transition. If at least two order parameters coexist in the same phase, the material is called a multiferroic [1]. The order parameter(s) can point in at least two symmetrically equivalent directions (polarities) between which it can be switched by the application of an external

This article has previously been published in the journal Physical Sciences Reviews. Please cite as: Evans, D. M., Garcia, V., Meier, D., Bibes, B. Domains and domain walls in multiferroics *Physical Sciences Reviews* [Online] 2020, 5. DOI: 10.1515/psr-2019-0067

https://doi.org/10.1515/9783110582130-011

field. When cooling through the phase transition in zero-field, the polarities have the same energy and, as a consequence, both polarities appear inside the ferroic material. Regions with the same polarity are called domains and the interfaces that separate them are call domain walls. While this shows, trivially, that multiple domains form naturally in ferroics, the details of how many domains, their size, and where they form, depend on several energy terms, as well as the local defect structure. In the following, we will give a brief outline of how ferroic domains and domain walls form, using a ferroelectric as an illustrative example; although, as we will see, analogous arguments can be made for the formation of domains and domain walls in ferromagnets. For more complete and in-depth descriptions of the physics of ferroelectric and ferromagnetic domains we refer to, for instance, the textbooks by Tagantsev et al. [2] and by Hubert and Schäfer [3].

A proper ferroelectric is a material for which the spontaneous electric polarization plays the role of the primary symmetry breaking order parameter, which can completely describe the phase transition into the ferroic state [4, 5]. Practically, this means energy contributions related to this order parameter are very important in the system, particularly for the domain formation. For instance, in ferroelectrics, surfaces perpendicular to the ferroelectric polarization have bound charges that create a strong depolarizing field (Figure 11.1(a)). This field is a major driving force for domain formation: the depolarizing field can be minimized by either (i) screening the surface charges of the ferroelectric with surface adsorbates or metallic electrodes (Figure 11.1(b)), or (ii) the formation of ferroelectric domains, for example, 180° domains, so that the net polarization at the surface averages to zero (Figure 11.1(c)). The number and size of the ferroelectric domains that form will depend on the details of the boundary conditions (Figure 11.1(d)), such as crystal size, shape, orientation, local defect structure and, critically, the energy costs associated with

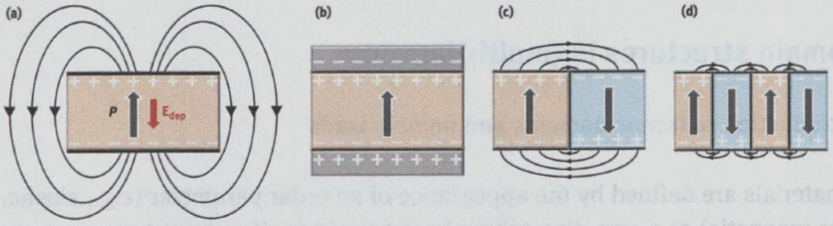

Figure 11.1: Domain formation in ferroelectrics. (a) Black field lines represent the electric stray field from a ferroelectric monodomain state. The grey arrow shows the polarization direction, $\boldsymbol{P}$. The build-up of stray electric fields induces a field in the opposite direction, the depolarizing field, $\boldsymbol{E}_{dep}$, indicated by the red arrow. (b) Complete screening of the ferroelectric polarization by surface charges. (c) 180° domain wall leading to a smaller electric stray field that reduces the internal depolarizing field. (d) Representative multidomain state showing the much smaller electric stray fields. Note that the number of domains formed will depend on several energy terms including the energy cost of having a domain wall, the size of the depolarizing field, and the presence of uncompensated surface bound charges.

the insertion of domain walls. Thus, depending on the boundary conditions, a thin ferroelectric film can either form a single-domain state or break into multiple nano-domains [2, 6], which has been used to engineer ferroelectric domains [7–10]. This can easily be observed by half covering a large single crystal with electrodes and cooling the sample through its Curie temperature: the area under the electrodes will form larger domains than the uncovered area due to the presence of screening charges from the electrodes, while the area in air will have a finer domain structure due to the depolarizing fields (see, e.g. Gilletta [11]). Importantly, from these simplistic arguments, it can be seen that the formation of domains and domain walls is a natural property of any ferroic crystal. Note that this applies in the case of zero applied electric field. Applying an electric field will affect both the transition temperature and the domain formation, see e.g. Merz [12].

In general, the size of the domains that form can be predicted by what is now known as Kittel's scaling law [13, 14]. Although Kittel attributed the original idea of size effects of domains to Frenkel and Doefman [15], it was Kittel's work on ferromagnets that provided the scaling relationship that now bears his name: the domain width is inversely proportional to one over the square root of their thickness as detailed below. Originally, his mathematical formalism considered only three contributions to the free energy as relevant, i.e., the surface energy of a domain wall, the magnetic field energy of the configuration, and the anisotropy of the spin orientation. Kittel's work on ferromagnets was then expanded to ferroelectrics by Mitsui and Furuichi in 1952 [16], showing that the fundamental scaling remains the same. It has also now been experimentally verified in ferroelectrics and multiferroics down to tens of nanometre sample thicknesses [17, 18]. Some corrections to Kittel's law have been proposed by Scott [19] due to the finite size of domain walls, being particularly pertinent in ferroelectrics, where domain walls are usually about one order of magnitude thinner than in ferromagnets.

To illustrate Kittel's scaling law, we consider the simple case of open boundary conditions without surface screening in a film with 180° striped-domains as illustrated in Figure 11.1(d). Here, the size of domains is determined by the competition between the energy of the domains and that of domain walls. The energy density, E, of the domains depends on their width, ω, as $E = U\omega$, where U is the volume energy density. The energy density of the domain walls depends on their number and so will be inversely proportional to ω as $E = \sigma d/\omega$, where σ is the energy density per unit area of the wall and d the thickness of the film. Minimizing the total energy gives rise to a square-root dependence of the domain size with the film thickness as $\omega = \sqrt{\sigma/U \times d}$, known as Kittel's law [14].

In the original form proposed for ferromagnets, it is the competition between magnetic exchange energy and demagnetizing field contributions that drives the domain formation: the magnetic exchange energy is minimized in single-domain states while the competing demagnetizing field favours the formation of multidomain states. Furthermore, additional factors arise from the size and shape of the

magnetic domains and domain walls, which will depend on the magnetocrystalline and magnetostrictive energies of the system. While the magnetic exchange energy favours wide walls, so that neighbouring magnetic moments are almost parallel to each other, magnetocrystalline anisotropy promotes narrow walls so that almost all the magnetization of the system is aligned with the easy magnetic axis. As a result, the thickness of these magnetic domain walls depends strongly on material parameters, but typical values are in the order of a few tens of nanometres and up to hundreds of nanometres [20]. In contrast to ferromagnets, where the exchange energy is much larger than the magnetocrystalline anisotropy, in ferroelectrics the anisotropy and dipole–dipole interactions (the equivalent of exchange in these materials) are of the same order of magnitude [21]. As a consequence, ferroelectrics usually develop much thinner walls than ferromagnets, with typical thicknesses in the order of a few unit cells (see, for instance, Refs [17, 22–26]). The smaller width of ferroelectric domain walls compared to magnetic domain walls implies that the order parameter changes orientation much faster.

At the domain wall itself there are, conceptually, three different ways for the polar order to change, referred to as Ising-, Bloch-, and Néel-type walls. The three domain wall types are schematically illustrated in Figure 11.2. In Ising-type walls (Figure 11.2(a)), the axis along which the order parameter points is fixed. Across the wall, only the magnitude of the polar order changes smoothly from up to down, going through zero at the centre of the wall. These walls are generally the thinnest

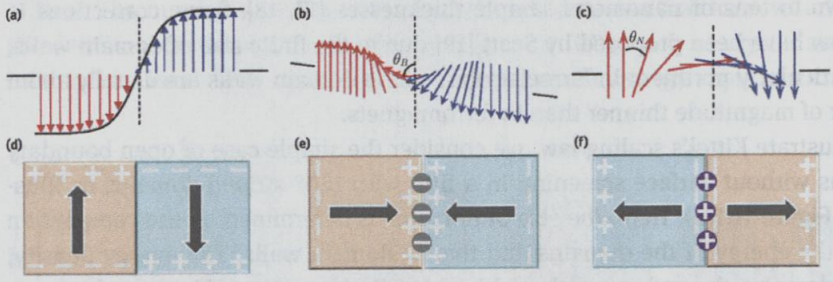

Figure 11.2: Fundamental types of ferroic domain walls. Arrows represent the orientation of the order parameter (e.g., polarization or magnetization). (a) Ising-type wall: the polarization/magnetization does not rotate but decreases in magnitude through the wall. (b) Bloch-type wall: the polarization/magnetization does not change magnitude but rotates in the plane of the domain wall. (c) Néel-type wall: the polarization/magnetization does not change magnitude, but rotates perpendicular to the plane of the domain wall. ((a)–(c) are reprinted with permission from [27]. Copyright 2009 by the American Physical Society.) (d)–(f) Charge states at ferroelectric 180° walls. (d) Neutral 180° domain wall. Positive and negative bound charges are denoted by symbols + and –, respectively. (e) Head-to-head domain wall, where the polar discontinuity associated with the positive domain wall bound charges attracts mobile negative charge carriers (grey). (f) Tail-to-tail domain wall, where the polar discontinuity associated with the negative domain wall bound charges attracts mobile positive charge carriers (purple).

of order (sub)nanometre wide. Traditionally, it was assumed that 180° domain walls in ferroelectrics are Ising-type walls, but recent experimental and theoretical work has revealed domain walls with more complex structures (see, e.g., Refs [27–30]). For ferroelectric Ising-type walls, as already mentioned above, both the anisotropy and dipole–dipole interactions are usually strong, and the energy difference between the paraelectric and ferroelectric phases is relatively small. Consequently, an abrupt change of polarization through the wall can readily be accommodated by a reduction of the magnitude of polarization as presented in Figure 11.2(a).

In the Bloch-type wall, the order parameter does not change size but rotates within the plane of the wall (Figure 11.2(b)). The Néel-type wall is characterized by a rotation of the order parameter perpendicular to the domain wall and at the wall centre the respective vector lies orthogonal to the plane of the domain wall (Figure 11.2(c)). Bloch- and Néel-type walls are most common in ferromagnets, where the energy difference between paramagnetic and ferromagnetic phases is large and, hence, the magnitude of magnetic moments does not vary significantly [3]. These magnetic domain walls can be quite wide and extend up to hundreds of nanometres in width [20]. The three extreme cases shown in Figure 11.2(a) to (c) are normally combined to describe domain walls in real systems, leading to mixed-type domain wall states. As already mentioned, it is important to note that Bloch- and Néel-type walls are not restricted to ferromagnets and, recently, there is a growing interest in non-Ising-type domain walls in ferroelectrics and the emergence of walls of Néel- and Bloch-type has been reported for different ferroelectric materials [31], such as $BaTiO_3$ [32] and $Pb(Zr,Ti)O_3$ (PZT) [33–35]. Note that the illustrations in Figure 11.2 are for domain walls at which the order parameter orientation changes by 180°; the details change for other situations, e.g., for 90° walls, but the salient points remain true.

In multiferroics, the situation becomes even more interesting as electric and magnetic domains and domain walls coexist (see, e.g., [36–41]), giving rise to unusual magnetoelectric correlation phenomena as discussed in Section 11.2 and 11.3 and also Chapter 3 and Chapter 4. Because of the coexistence of different types of ferroic order in multiferroics, it becomes important to consider whether the polarization or magnetization plays the role of the symmetry breaking order parameter and, thus, governs the formation of domains and domain walls. In this context, one typically distinguishes between proper and improper systems or, more precisely, between systems in which the ferroic order arises across a proper or improper phase transition [4, 5, 42]. For example, as described above, a ferroelectric phase transition is referred to as proper, if the spontaneous polarization is the primary symmetry breaking order parameter that drives the transition. This is the case in textbook ferroelectrics, such as $BaTiO_3$, PZT, and $LiNbO_3$ [2, 43]. Alternatively, electric order can arise as a secondary effect driven by the coupling to, e.g., a structural [44–47] or magnetic order parameter [48–50] as reviewed, e.g., in Ref [40]. The latter scenario, referred to as improper ferroelectricity (or pseudo-proper; see, e.g., [4, 42] for details), is realized

in many multiferroics, such as the hexagonal manganites ($RMnO_3$, with R = Sc, Y, In, Dy to Lu; reviewed in Chapter 3) and orthorhombic $TbMnO_3$ and $DyMnO_3$, with fascinating consequences for the domain walls [39, 51–53]. Here, due to the secondary nature of the spontaneous polarization, exotic *charged* domain walls (Figure 11.2(e) and (f)) arise spontaneously – a situation that is usually avoided due to the high electrostatic energy costs.

Assuming an Ising-type wall, a domain wall is said to be fully charged if the polarization of neighbouring domains comes together head-to-head or tail-to-tail as shown in Figure 11.2(e) and Figure 11.2(f), respectively. The associated discontinuity in polarization $\boldsymbol{P}$ leads to uncompensated domain wall bound charges (div $\boldsymbol{P} \neq 0$), which require screening (see, e.g., [54] and references therein). As a consequence, mobile carriers redistribute, promoting anomalous electronic transport properties at head-to-head and tail-to-tail walls, including highly conducting and insulating states as reviewed in [54–56], as well as the formation of unusual electronic inversion layers [57]. Charged domain walls thus represent a natural type of two-dimensional system with inherent functional properties, which can be injected, moved and erased on demand [55, 58–61]. Additional functionalities arise at domain walls with a strong coupling between electric and magnetic degrees of freedom, enabling magnetic-field control of the local electronic charge state as discussed in Section 11.3 [36, 39]. For a more comprehensive or more technical coverage of charged domain walls in ferroelectrics and multiferroics, we refer to recent reviews [40, 56, 62, 63], and the specific studies highlighted in the following sections.

11.1.2 Visualization of domains

The rapid progress that has been made in the understanding of magnetic and electric domains relies on the recent developments in microscopy techniques with high sensitivity and unprecedented spatial resolution. Nowadays, even atomic level resolution is readily available with transmission electron microscopy (TEM) (see, e.g., Chapter 7 or [64], as well as references therein). In this review, we discuss different microscopy methods that allow for studying the formation and interaction of ferroic domains in spatially resolved measurements on nano- to microscopic length scales. In multiferroics, a specific difficulty arises for domain imaging as one needs to distinguish contributions from at least two coexisting types of ferroic order. Many available techniques, however, are simultaneously sensitive to both magnetism and ferroelectricity, making the distinction between the two signals challenging. For instance, photoemission electron microscopy (PEEM) based on X-ray linear dichroism (XLD) is sensitive to the asymmetry of the electronic charge distribution and, hence, to contributions from both ferroelectric and antiferromagnetic domains. Another example is scanning probe microscopy (SPM); the magnetic tip used for magnetic force

magnetometry (MFM), for example, will probe contributions from the stray field of the magnetic domains as well as the electrostatic fields from the ferroelectric domains and surface charges (as in electrostatic force magnetometry (EFM)). In the following, we give examples of different techniques with which magnetic and ferroelectric domains can be observed independently as illustrated based on measurements taken on both intrinsic and artificial multiferroics (Figure 11.3).

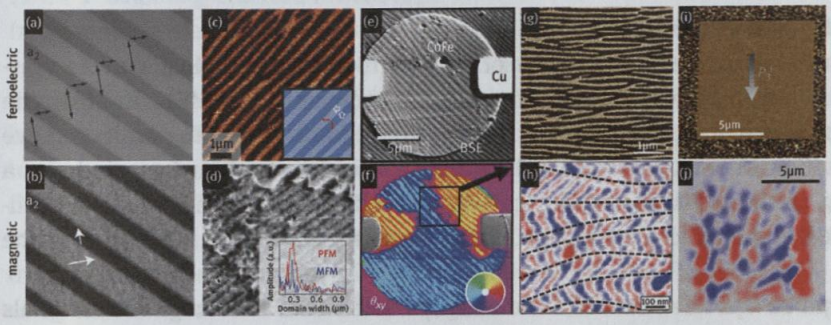

Figure 11.3: Imaging magnetic and ferroelectric domains in artificial and intrinsic multiferroics. (a) Polarized optical microscopy image of (a) the a1-a2 birefringent ferroelectric domains of a $BaTiO_3$ single crystal and (b) the magnetic domains of the uniaxial $Co_{0.6}Fe_{0.4}$ layer (15 nm) grown on top. ((a) and (b) are from [65]). (c) PFM image of a $BiFeO_3$ film grown on a $DyScO_3$(110) substrate and (d) MFM image on the same sample after the growth of a $Pt/Co_{0.9}Fe_{0.1}$ bilayer on top under a magnetic field of 20 mT. In the inset, the Fourier analysis indicates the correlation between the PFM and MFM patterns. ((c) and (d) are reprinted with permission from [66]. Copyright 2013 by the American Physical Society.) (e) Ferroelectric domain structure of $BiFeO_3$ imaged using the back-scattered electron (BSE) intensity with a $Co_{0.9}Fe_{0.1}$ thin-film circular disk and Cu electrode on the side. (f) Simultaneously acquired SEMPA image of the magnetic structure. The magnetization direction is represented by colours as indicated by the colour wheel. ((e) and (f) are reprinted with permission from Springer Nature, taken from [67]. Copyright 2015 by Springer Nature.) (g) In-plane PFM image of the striped-domain structure of a 30-nm-thick $BiFeO_3$ thin film grown on $DyScO_3$(110) and (h) NV-magnetometry image of the stray field produced by the spin cycloid of the same film. ((g) and (h) reprinted with permission from Springer Nature, taken from [68]. Copyright 2017 by Springer Nature.) (i) In-plane PFM image of a single ferroelectric domain written with the trailing field of the SPM tip on a $BiFeO_3$ thin film grown on a $SrTiO_3$(001) substrate. (j) Reconstructed SHG image showing two types of submicron antiferromagnetic domains in the ferroelectric domain showed in (i). ((i) and (j) reprinted with permission from Springer Nature, taken from [69]. Copyright 2017 by Springer Nature.)

11.1.2.1 Optical microscopy

In bulk single crystals, domains may reach sizes in the micron range compatible with optical microscopy. In this case, ferroelectric domains can be imaged with the birefringent contrast [70–72] or selective etching [73], while magnetic domains on this length scale are observed via the magneto-optical Kerr effect. Figure 11.3(a), (b) illustrates this on an artificial multiferroic system based on a thin ferromagnetic

film (15 nm of $Co_{0.6}Fe_{0.4}$) deposited on a ferroelectric single crystal ($BaTiO_3$) [65]. The ferroelectric domains of $BaTiO_3$ organize in the form of stripes with 90° ferroelastic domain walls (a1-a2 domains corresponding to in-plane polarization in Figure 11.3(a)). Strain coupling between the $Co_{0.6}Fe_{0.4}$ thin film and the underlying $BaTiO_3$ single crystal induces uniaxial magnetoelastic anisotropy with orthogonal easy axes between neighbouring domains, resulting in an imprinted stripe pattern (Figure 11.3(b)).

11.1.2.2 Scanning probe microscopy

SPM allows nanoscale investigation of both ferroelectric domains, via piezoresponse force microscopy (PFM), and ferromagnetic domains, via MFM. In MFM, the magnetic tip experiences an attracting or repelling force depending on its relative magnetization orientation compared to that of the sample. This force induces a phase lag on the oscillation of the tip that is coverted into a map so that MFM images reveal the spatial distribution of the magnetic stray field coming from the sample.

The probe tips used for MFM are usually coated with ferromagnetic materials and their metallicity enables their subsequent use for PFM. PFM uses the fact that all ferroelectric materials are piezoelectric. By applying an alternating voltage between the SPM tip and the ferroelectric in contact, the ferroelectric will vibrate at the same frequency as the voltage excitation. In the ideal case, the phase shift of the response is directly connected to the out-of-plane polarization orientation of the ferroelectric (see, e.g., [74] for a recent review on PFM). In the same manner, the torsion of the tip contains information on the in-plane components of the polarization. An example is given in Figure 11.3, where the MFM contrast coming from a 2.5-nm-thick $Co_{0.9}Fe_{0.1}$ amorphous layer (Figure 11.3(d)) is correlated to the PFM contrast from the ferroelectric domain pattern (Figure 11.3(c)) in the underlying layer of $BiFeO_3$ [66]. In this configuration, the surface bound charges of $BiFeO_3$ are screened by the magnetic top electrode and the MFM signal is "pure". This correlation attests for the coupling between the ferromagnetic domains in $Co_{0.9}Fe_{0.1}$ and the antiferromagnetic domains in $BiFeO_3$, the latter being magnetoelectrically coupled with the ferroelectric order.

In order to directly image the magnetic stray field coming from the antiferromagnetic domains in multiferroics, such as $BiFeO_3$ (see Chapter 2 for details on $BiFeO_3$), a scanning probe technique with higher sensitivity than MFM is required. Recently, scanning nitrogen-vacancy (NV) magnetometry was developed in which magnetic stray fields down to a few μT can be detected [75]. In bulk [76] and lightly strained films of the antiferromagnetic $BiFeO_3$ [77], the magnetoelectric interaction stabilizes the formation of a spin cycloid – originally probed by Sosnowska et al. using neutron diffraction [78] – whose propagation vector is coupled to the polarization direction. Gross et al. were able to use NV magnetometry to visualize

the magnetic stray field emanating from this 70-nm-long spin cycloid (Figure 11.3 (h)) in striped domain patterns of $BiFeO_3$ thin films [68] (Figure 11.3 (g)). The in-plane compressive strain imposed by the $DyScO_3$ substrate lifts the degeneracy between the three possible propagation vectors for the spin cycloid for each ferroelectric domain, resulting in the in-plane 90° rotation of the magnetic signal between alternating ferroelectric domains (Figure 11.3 (h)).

11.1.2.3 Scanning electron microscopy

In a scanning electron microscope with polarization analysis (SEMPA), the low energy secondary electrons are spin-polarized and give information on the magnetization orientation of the ferromagnetic structure, while the high energy elastically back-scattered electrons (BSE) are sensitive to the crystal structure and lattice distortions to reveal the polarization orientation of the ferroelectric structure. Combining SEMPA and BSE, Zhou et al. were able to simultaneously image the local in-plane vector magnetization of the $Co_{0.9}Fe_{0.1}$ layer (Figure 11.3(f)) grown over the striped-domain ferroelectric structure of $BiFeO_3$ (Figure 11.3(e)) [67]. The comparison of the SEMPA and BSE images shows the close correlation between the magnetic structure of the $Co_{0.9}Fe_{0.1}$ film and the striped ferroelectric domain structure of the underlying $BiFeO_3$ layer. Within a stripe, which is about 250 nm wide, the magnetization is aligned parallel or anti-parallel to the in-plane surface projection of the electric polarization.

11.1.2.4 Photoemission electron microscopy

A possible way to discriminate ferroelectric and magnetic domain contrasts is to take advantage of the potentially different Curie and Néel temperatures of the multiferroic. This approach was used by Zhao et al. [79] to distinguish the antiferromagnetic contribution and the ferroelectric one in photoemission electron microscopy (PEEM) images of $BiFeO_3$ thin films. A careful comparison of the PEEM contrast under and above the Néel temperature of $BiFeO_3$ ($T_N = 640$ K) allows for separating the "pure" ferroelectric contrast from the multiferroic one with a resolution down to ≈20 nm. A smart combination of XMLD- (X-ray magnetic linear dichroism) and XMCD- (X-ray magnetic circular dichroism) PEEM imaging (mapping spin and orbital magnetic moments) is a very powerful tool.

11.1.2.5 Second harmonic generation

Second harmonic generation (SHG), that is, the frequency doubling of light in a material, is a powerful technique to sense complex magnetic and electric structures [41, 80, 81]. It is well suited to probe insulators with a spatial resolution in the submicron range limited by the wavelength of the light. In bulk multiferroics, SHG domain imaging was pioneered by Fiebig [41]. More recently, Chauleau et al. used

SHG to probe antiferromagnetic domains across a ferroelectric single-domain of a $BiFeO_3$ thin film (Figure 11.3(i)) [69]. They performed the experiments in transmission while varying the incident polarization of the light and analyzed the full angular dependence of each pixel. The 110-nm-thick $BiFeO_3$ thin film was epitaxially grown on $SrTiO_3(001)$ at a compressive strain that destroys the cycloidal spin structure and stabilizes a slightly-canted antiferromagnetic state arising from the Dzyaloshinskii–Moriya interaction [77]. In this G-type antiferromagnetic system, the Fe^{3+} spins are aligned along three possible antiferromagnetic vectors of the (111) plane, perpendicular to the ferroelectric polarization. As depicted in Figure 11.3(j), only two types of submicron antiferromagnetic domains were observed in this single $BiFeO_3$ ferroelectric domain, suggesting that the magnetoelastic energy lifts the degeneracy between the three types of antiferromagnetic domains.

11.1.2.6 Combined imaging experiments

While the application of just one experimental method that can image both electric and magnetic domains is clearly intriguing, the majority of studies on multiferroics still make use of two or more complementary techniques to image the coexisting domains and domain walls and cover all relevant length scales. The latter is nicely reflected by the research studies on multiferroics involving PFM. PFM by itself provides access to the distribution of ferroelectric domains. The combination of PFM with PEEM and X-ray resonant magnetic scattering led to the discovery of coupled ferroelectric and ferromagnetic domains in $BiFeO_3$ thin films [79] and interfacial multiferroicity in $Fe/BaTiO_3$ and $Co/BaTiO_3$ heterostructures [82]. PFM in combination with NV magnetometry disclosed the coupling between ferroelectric and antiferromagnetic domain in $BiFeO_3$ [68] (see also Section 11.3). In addition, PFM has been combined with many other methods such as TEM, optical microscopy, as well as SHG in order to understand and disentangle the formation of electric and magnetic domains in different multiferroic materials. For a more extended review on PFM, see [74].

11.2 Domain walls in multiferroics

The recent discovery of functional electronic and magnetic properties at multiferroic domain walls triggered world-wide attention and initiated a shift in the research focus away from domains and towards domain walls. The domain wall research is driven by the idea to develop a new generation of agile interfaces/2D systems that remain spatially mobile after a material has been synthesized and implemented into a device structure [55]. Going beyond just conducting domain walls, as observed in ferroelastic and ferroelectric materials, multiferroics offer additional degrees of freedom that arise from the magnetic order and the unusual couplings between their electric, magnetic and structural properties as discussed in the following.

11.2.1 Domain wall types

Across domain walls in multiferroics, one or more order parameters change from one direction to another and this can occur in many different ways depending on the type of involved ferroic orders, the direction of the order parameters in the adjacent domains (e.g., parallel or perpendicular to the wall), and the geometry and dimensions of the sample [83, 84]. The range of structures that arises within a domain wall in the presence of just one order parameter has already been addressed in Section 11.1 (see Figure 11.2). In order to classify the complex domain walls that occur in multiferroics with coexisting electric and magnetic order [24, 62, 85], a first distinction can be made based on the interaction of the respective domain walls as shown in Figure 11.4(a) and Figure 11.4(b) [40].

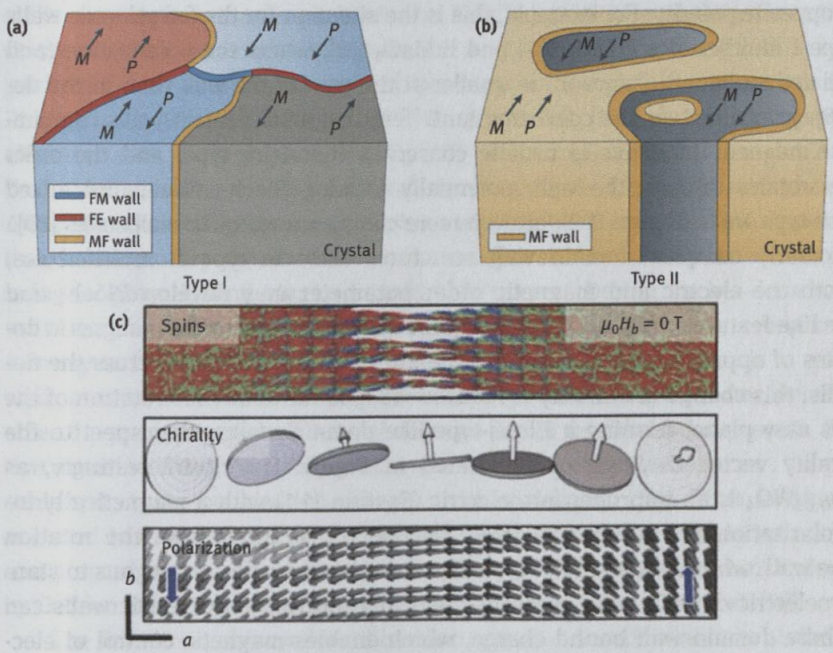

Figure 11.4: Domain walls in multiferroics. (a) In type I multiferroics magnetic and electric order emerge independently and so do not need to coincide. This gives domain walls which are either magnetic (blue) or electric (red) in nature. If the domains happen to coincide, then a multiferroic (orange) wall is formed, which points to a coupling that is not required by symmetry. (b) In type II multiferroics the magnetic order induces the electric order. Thus, ferroelectricity emerges at the magnetic phase transition. Due to this interdependence of order parameters, all ferroelectric domain walls are also magnetic domain walls and therefore multiferroic walls. ((a)–(b) are reprinted with permission from Springer Nature, taken from [40]. Copyright 2016 by Springer Nature.) (c) Landau–Lifshitz–Gilbert simulation showing the complex evolution of spins (top), the spin chirality (middle), and electric polarization (bottom) across a multiferroic domain wall in $Mn_{0.95}Co_{0.05}WO_4$. (Reprinted with permission from Springer Nature, taken from [36]. Copyright 2015 by Springer Nature.)

In multiferroics where electric and magnetic orders occur independently (type I), electric and magnetic domain walls can coincide, but they do not necessarily have to couple due to the different microscopic origin of the polarization (P) and magnetization (M) (Figure 11.4(a)). This is different in systems where the magnetic order induces the spontaneous polarization (see also Chapter 4), or vice versa, so that both orders occur together (type II, Figure 11.4(b)). In the latter case, every ferroelectric domain wall is also a magnetic domain wall [37, 86], representing a two-dimensional system with multiferroic properties different from the surrounding bulk.

A second, more advanced distinction is related to the conservation (or not) of the amplitude of the order parameter(s) across the wall. As introduced in Section 11.1, we usually consider three fundamental types of ferroic domain walls, namely, Ising-, Néel-, and Bloch-type walls (Figure 11.2). For Ising-type walls, upon crossing the wall the order parameter decreases, becomes zero at the centre and then increases again with the opposite polarity. For example, this is the situation for the ferroelectric walls in the type I multiferroics $BiFeO_3$ [87] and $ErMnO_3$ [22], where the polarization (and the associated structural distortion) is smaller at the core of the wall than in the domains [88]. In contrast, at the coexisting (anti-)ferromagnetic domain walls, the amplitude of magnetic moments is usually conserved (non-Ising-type) and the order parameter rotates through the wall, potentially forming Bloch-, Néel-, and mixed Néel-Bloch-type walls (Figure 11.2), or even more complex vortex-like wall states [89].

Particularly complex domain wall structures arise in type II multiferroics, where both the electric and magnetic order parameter may develop Bloch- and Néel-type like features. In $Mn_{0.95}Co_{0.05}WO_4$, for instance, two antiferromagnetic domain states of opposite chirality occur in the multiferroic state [36]. Across the domain walls, this change in chirality is realized via a continuous 180° rotation of the material's easy-plane, forming a Bloch-type-like domain wall with respect to the spin-chirality vector $C = S_i \times S_j$ as illustrated in Figure 11.4(c). Interestingly, as $Mn_{0.95}Co_{0.05}WO_4$ is an improper ferroelectric (Section 11.1) with a magnetically induced polarization ($P \sim e_{ij} \times (S_i \times S_j)$ [49]), the electric order follows the rotation across the wall, which leads to Néel-type-like ferroelectric walls. Analogous to standard ferroelectric domain walls, such magnetically induced ferroelectric walls can carry a finite domain wall bound charge, which enables magnetic control of electronic domain wall states as we discuss in more detail in Section 11.3.

In summary, pronounced couplings between the electric and magnetic order parameters can occur in multiferroics, giving rise to a huge richness of domain wall structures and properties. Although the electric dipole and magnetic spin configurations at the atomic scale are rarely available – so that the exact wall types often remain unknown – it is clear that multiferroic domain walls can show unexpected and fascinating physical properties beyond the bulk properties. Today, we are only at the verge of discovering these exciting properties. Novel findings and insight into the nano-physics of domain walls are to be expected in the near future, enabled by the continuous and

ongoing progress in advanced microscopy techniques. Some of the recent key results in the field are reviewed in the following.

11.2.2 Conduction in domain walls

A little history – The emergence of conducting domain walls was postulated first in the 1960s and 70s based on macroscopic measurements in classic ferroelectrics like TGS (triglycine sulfate), $PbTiO_3$, $BaTiO_3$, $LiNbO_3$, and SbSI [90–94]. Due to experimental limitations of the time, however, it was not possible to measure individual walls directly. Aristov et al. were among the first to spatially resolve domain walls with anomalous electronic properties in ferroelectric $BaTiO_3$ [95] and, later, also in $LiNbO_3$ [96] using scanning electron microscopy [97]. The first direct evidence of conducting domain walls was in pioneering experiments on $BiFeO_3$ by Seidel et al. [87]. Since then, conductance measurements using conductive atomic force microscopy (cAFM) have been performed on a diverse range of prototypical (proper) ferroelectrics, including $PbZr_{0.2}Ti_{0.8}O_3$ [98–100], $LiNbO_3$ [101–103], and $BaTiO_3$ [104], as well as improper ferroelectrics, such as hexagonal $RMnO_3$ [105–109], $Cu_3B_7O_{13}Cl$ [110], and $(Ca,Sr)_3Ti_2O_7$ [111], demonstrating that domain wall conductivity is a quite general phenomenon. Although conducting domain walls have already been analyzed and discussed more than half a century ago, only the recent in-depth studies have revealed their full technological potential and triggered world-wide interest. During the last decade, domain-wall-based multi-configurational devices, atomic-scale electronic components and memory technology have been proposed [58, 112, 113]. Another idea is to use domain walls in order to achieve reconfigurable doping: While semiconductor technology enables the precise control of charged dopants during the fabrication process, their location remains fixed. Reconfigurable channels of charge carriers are, in principle, achievable using polarization charges as quasi-dopants [114]. Then, doping may be achieved in ferroelectrics within the domain walls. For more insight into the physics and properties of ferroelectric domain walls, we refer to, e.g., the recent review articles by Catalan et al. [55], Meier [54], Jiang et al. [113], and Bednyakov et al. [56].

The first direct observation of conductivity at a domain wall was also the first in a multiferroic: Seidel et al. observed room-temperature conduction at 180° and 109° domain walls in multiferroic $BiFeO_3$ thin films (Figure 11.5(a), (b)), while no conduction could be detected at 71° domain walls [87]. This seminal paper triggered a plethora of experimental and theoretical works on conductive domain walls partly fuelled by the controversy regarding the origin of these effects. The initial interpretation from Seidel et al., supported by density functional theory (DFT), suggested that electrostatic potential steps at the domain walls were responsible for the enhanced conduction, as well as a reduced bandgap induced by structural transitions in the wall. In addition, DFT calculations showed that these effects were minimized for 71° domain walls in agreement with experiments. However, following reports concluded

that the conduction through these neutral walls was mostly related to extrinsic contributions [83, 115]. Farokhipoor & Noheda found that 71° domain walls were also conducting in $BiFeO_3$ thin films (Figure 11.5(d), (e)) [115]. Through a temperature analysis of the conduction, they demonstrated that it is governed by thermally activated transport from defects (oxygen vacancies) at low voltage (Figure 11.5(f)) and Schottky emission at higher voltage, just as for the domains. The different conduction for domains and domain walls is explained by an increased density of oxygen vacancies at the walls, giving rise to in-gap states and lower electron hopping energy. In the same vein, Seidel et al. reported that the oxygen pressure during the cool-down process after the growth of La-doped $BiFeO_3$ had a large influence on the 109° domain wall conduction, with a current increase by two orders of magnitude under low oxygen pressure (Figure 11.5(c)) [83].

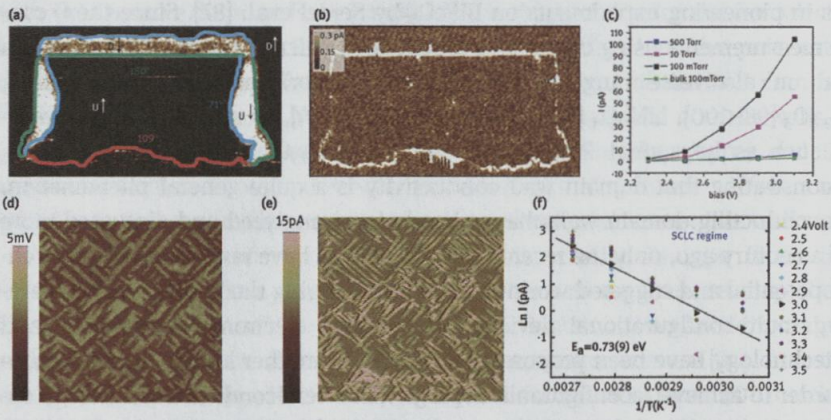

Figure 11.5: Conduction at charge-neutral domain walls in multiferroic $BiFeO_3$ thin films. (a) 109°, 180° and 71° domain walls in a (110)-oriented $BiFeO_3$ thin film observed by PFM and the corresponding (b) cAFM map showing enhanced conduction for 180° and 109° domain walls. ((a)–(b) reprinted with permission from Springer Nature, taken from [87]. Copyright 2009 by Springer Nature.) (c) Influence of the oxygen pressure after growth on the conduction of 109° domain walls in La-doped $BiFeO_3$ thin films. ((c) is reprinted with permission from [83]. Copyright 2010 by the American Physical Society.) (d) PFM amplitude of a (001)-oriented $BiFeO_3$ film with a majority of 71° domain walls and (e) corresponding cAFM image showing enhanced conduction at the domain walls. (f) Arrhenius plot of the current vs. temperature showing a thermally activated behaviour of the conduction through 71° domain walls. ((d)–(f) are reprinted with permission from [115]. Copyright 2011 by the American Physical Society.)

Somewhat easier and more straightforward to understand are electrostatics-driven contributions to the domain wall conductivity. At domain walls where the polarization meets either fully or partially in head-to-head or tail-to-tail configuration (see Figure 11.2(e), (f)), positive or negative domain wall bound charges exist, respectively, creating diverging electrostatic potentials. The compensation of the bound charge can be achieved by the redistribution of mobile charge carriers as we addressed

in Section 11.1. Though charged domain walls are not favoured in proper ferroelectrics, they naturally arise in various multiferroic materials. This abundance is due to the fact that multiferroics are often improper ferroelectrics (see Section 11.1 and 11.2), where the formation of domains is governed by, e.g., a structural or magnetic order parameter and not the electric polarization [40]. Multiferroic hexagonal manganites, $RMnO_3$, exhibit an intriguing ferroelectric domain pattern [106, 116] and are an interesting example for the natural emergence of both neutral [106, 117] and charged domain walls [57, 105, 118–121]: Here, a trimerizing lattice distortion leads to stable 180° charged domain walls with anomalous electronic transport properties (Figure 11.6 (a), (b)) [105, 119]. The extraordinary stability of these charged domain walls is reflected by recent electrostatic force microscopy measurements [122], which showed that partially unscreened walls arise at low temperature, representing a rare example of a stable, electrically uncompensated oxide interface (Figure 11.6(c)).

Meier et al. observed that in $ErMnO_3$, the conduction of the domain walls is a continuous function of the wall orientation (Figure 11.6(a)) [105]. Enhanced conductance was found at tail-to-tail walls while head-to-head walls showed a lower conduction than the domains (Figure 11.6(b)). This can be explained by the p-type semiconducting nature of $ErMnO_3$; here, mobile holes are available to screen the negative bound charges at tail-to-tail walls. The electrostatic potential at the walls shifts the Fermi level into the broad valence band where the effective mass is low, leading to an enhanced conduction at the walls [105]. In order to control and optimize the electronic domain wall properties in hexagonal manganites, effects related to off-stoichiometry [118, 123–128] and aliovalent cation substitution on the A- and B-site were studied systematically [129, 130]. Interestingly, recent studies suggest that the emergence of anomalous conductance is not restricted to isolated head-to-head and tail-to-tail walls in $RMnO_3$: Wherever the walls intersect in the characteristic cloverleaf-like arrangement [106, 116], ferroelectric vortex cores with emergent U(1) symmetry form [131–133]. These vortex cores are quasi-1D objects and exhibit quite unusual bound-charge distributions and electrostatics (Figure 11.6(d)), which – similar to the charged walls – is likely to change the electronic transport properties locally [22].

The results highlighted here, however, represent only a fraction of the research devoted to the domain and domain wall physics in hexagonal manganites. Due to the stability and abundance of charged domain walls, the material has become an important model system for the theoretical and experimental study of the complex nano-physics of functional domain walls and different application opportunities as nanoscale digital switches and half-wave rectifiers have been proposed [57, 108].

The majority of envisioned domain wall applications in nanoelectronics, such as domain-wall-based memories and multi-configurational devices, however, require highly mobile domain walls that can readily be injected and deleted at will. The intentional creation of charged domain walls was first demonstrated in 2013 in ferroelectric $BaTiO_3$ single crystals [104]. The stabilization of 90° charged domain

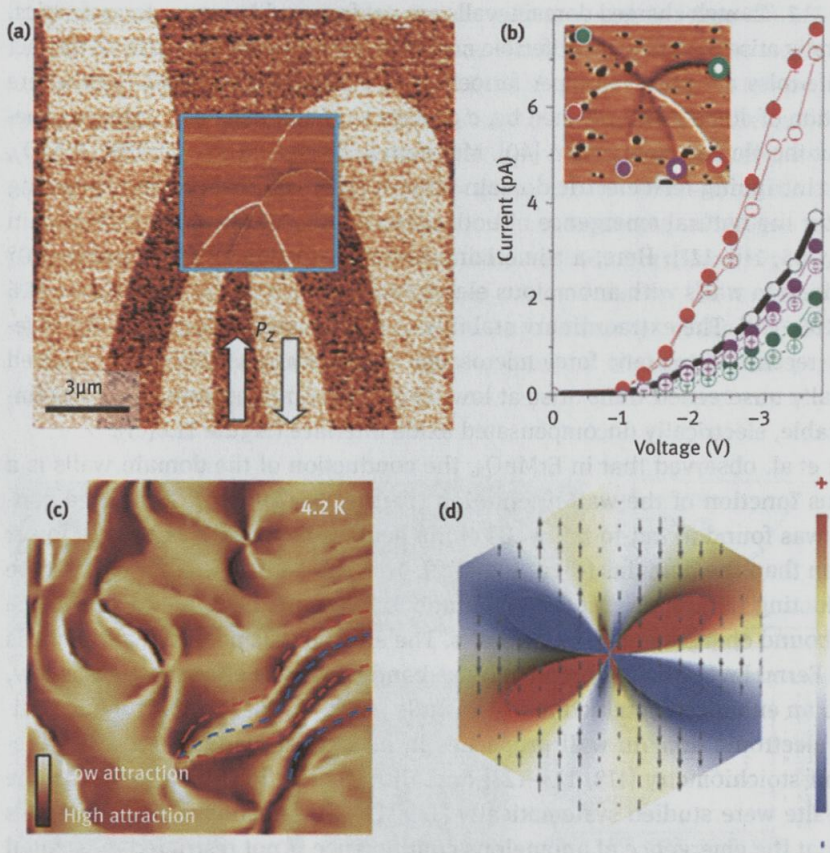

Figure 11.6: Charged domain walls in hexagonal manganites. (a) PFM image in the yz-plane of an $ErMnO_3$ single crystal. The inset shows a cAFM map recorded in the same region. The bright and dark lines show that domain walls have enhanced and reduced conduction relative to the domains, respectively. (b) Local current-voltage characteristics obtained at the locations shown in the inset. Tail-to-tail walls (red) show an enhanced conduction while head-to-head walls (purple and green) are less conducting than the domains (black). (reprinted with permission from Springer Nature, taken from [105]. Copyright 2012 by Springer Nature.) (c) EFM image of $Er_{0.99}Ca_{0.01}MnO_3$ taken at 4.2 K, showing the different fields (imaged as high/low attraction) arising from partially uncompensated charges at domain walls. (Reprinted with permission from [122]. Copyright 2019 American Chemical Society.) (d) Density plot of the bound-charge distribution emerging from the centre of a vortex core in the hexagonal manganites; the arrows indicate the direction of ferroelectric polarization. ((d) is taken from [22] and reused with permission from ACS. All further permissions must be directed to ACS.)

walls was realized by cooling down the single crystal under a strong electric field from above the Curie temperature. Then, the authors compared the conduction of individual head-to-head and tail-to-tail domain walls with the domains by contacting them with 200-micron-wide metallic electrodes (Figure 11.7(a)). While the conduction

at tail-to-tail walls was comparable to that of domains, a conduction 10^4 to 10^6 times higher than in the domains was observed at head-to-head domain walls (Figure 11.7(b)) with a metallic character (Figure 11.7(c)). However, this frustrated poling process is not technology transferrable for the realization of reconfigurable devices based on ferroelectric and multiferroic thin films. In 2015, Crassous et al. succeeded in creating charged walls, using the trailing field of the SPM probe tip (similar to Balke et al. [134]) to design charged ferroelastic domain walls in a multiferroic thin film, this time using La-doped $BiFeO_3$ grown on $DyScO_3(110)$ orthorhombic substrates (Figure 11.7(d)) [114]. CAFM maps of the artificial domains revealed a remarkable enhancement of the conductivity at head-to-head domain walls only (Figure 11.7(e)) with unprecedently high currents (two orders of magnitude higher than previous reports with neutral walls). Moreover, temperature-dependent measurements indicated a metallic behaviour for these charged walls as opposed to the thermally activated behaviour at neutral 71° domain walls (Figure 11.7(f)). On the other hand, ferroelectric tail-to-tail walls do not show a significant conduction as this configuration cannot be compensated by mobile holes, which gives rise to a roughening of the wall as well. In addition, the authors demonstrated

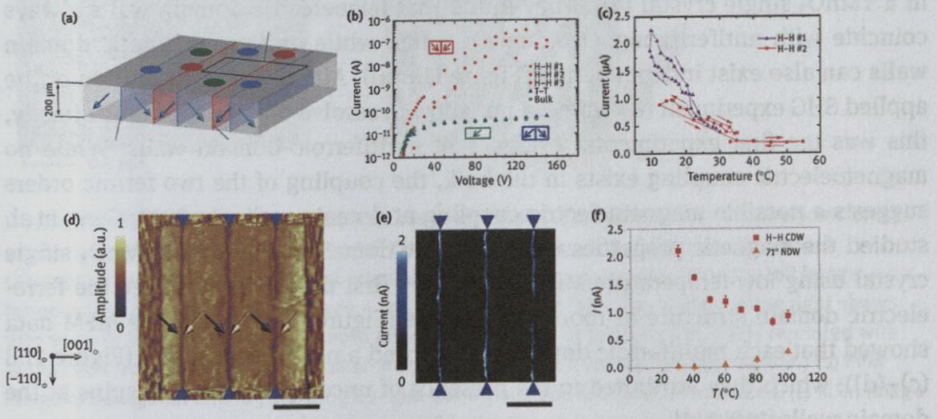

Figure 11.7: Conduction at created charged domain walls in ferroelectrics and multiferroics. (a) Sketch of the (110) $BaTiO_3$ crystal where the surface is covered with 200 µm diameter electrodes. The domain walls are irregularly distributed with periods from 100 to 300 µm. (b) Current-voltage characteristics of the tail-to-tail and head-to-head walls, as well as the domains. (c) Temperature dependence of the current through the head-to-head domain walls indicating a metallic behavior. ((a)–(c) are reprinted with permission from Springer Nature, taken from [104]. Copyright 2013 by Springer Nature.) (d) PFM amplitude of the domain pattern with alternating head-to-head and tail-to-tail domain walls defined by the trailing field of the SPM tip in La-doped $BiFeO_3$ thin films. (e) CAFM maps on the same domain pattern show an enhanced conduction at the head-to-head domain walls. The scale bars in (d) and (e) are 1 µm. (f) Temperature dependence of the current through the head-to-head walls compared to that of native 71° domain walls. ((d)–(f) are reprinted with permission from Springer Nature, taken from [114]. Copyright 2015 by Springer Nature.)

the reconfigurability of the writing process as well as the nanoscale manipulation of conductive head-to-head walls.

11.2.3 Magnetism at domain walls

In $BiFeO_3$, the coupling between ferroelectric and antiferromagnetic domain walls has been extensively investigated [135–137]. In $BiFeO_3$ thin films grown under high compressive strain, the rhombohedral-like phase and the tetragonal-like phase coexist in the form of nanoscale structures. Using XMCD-PEEM, Zhang et al. observed an enhancement of magnetism at the nanoscale boundaries of these mixed-phase thin films [138]. The magnetotransport properties of these walls have also been investigated [139].

Domain wall magnetism and its correlation to the ferroelectric order was first investigated in hexagonal manganites. These materials order antiferromagnetically below a Néel temperature, $T_N \approx 100$ K, whereas ferroelectricity arises at much higher temperature, $T_C \approx 1000$ K (see, e.g., Chapter 3). Using SHG imaging at 6 K, Fiebig et al. were able to discriminate antiferromagnetic domains from ferroelectric domains in a $YMnO_3$ single crystal [41]. They found that ferroelectric domain walls always coincide with antiferromagnetic domain walls, while antiferromagnetic domain walls can also exist independently (Figure 11.8(a)). Although the resolution of the applied SHG experiment ($\gtrsim 1$ μm) did not allow to resolve the domain walls directly, this was the first experimental evidence of multiferroic domain walls. While no magnetoelectric coupling exists in the bulk, the coupling of the two ferroic orders suggests a possible magnetoelectric coupling at domain walls. In 2012, Geng et al. studied the magnetic properties of multiferroic domain walls in an $ErMnO_3$ single crystal using low-temperature MFM [140]. They first used PFM to image the ferroelectric domain structure at room temperature (Figure 11.8(b)) and the MFM data showed that each multiferroic domain wall carried a net magnetization (Figure 11.8 (c)–(d)), which they attributed to the presence of uncompensated Er^{3+} spins at the domain walls [140, 141].

Multiferroic domains and domain walls with explicitly strong coupling between the electric and magnetic order were discovered in the spin-spiral multiferroic $MnWO_4$ (type II) [37, 86]. In $MnWO_4$, hybrid ferroelectric/antiferromagnetic domains arise below 15 K (Figure 11.8(e), (f)) driven by an elliptical spin spiral that breaks the inversion symmetry and, thereby, induces improper ferroelectricity [142]. Because of the magnetic origin of the ferroelectric order, and in strong contrast to the hexagonal manganites, electric and magnetic domain walls always coexist in $MnWO_4$. The inner structure of these walls remains to be measured, but theory predicts that they are antiferromagnetic in nature, similar to the case illustrated in Figure 11.4(c) [36].

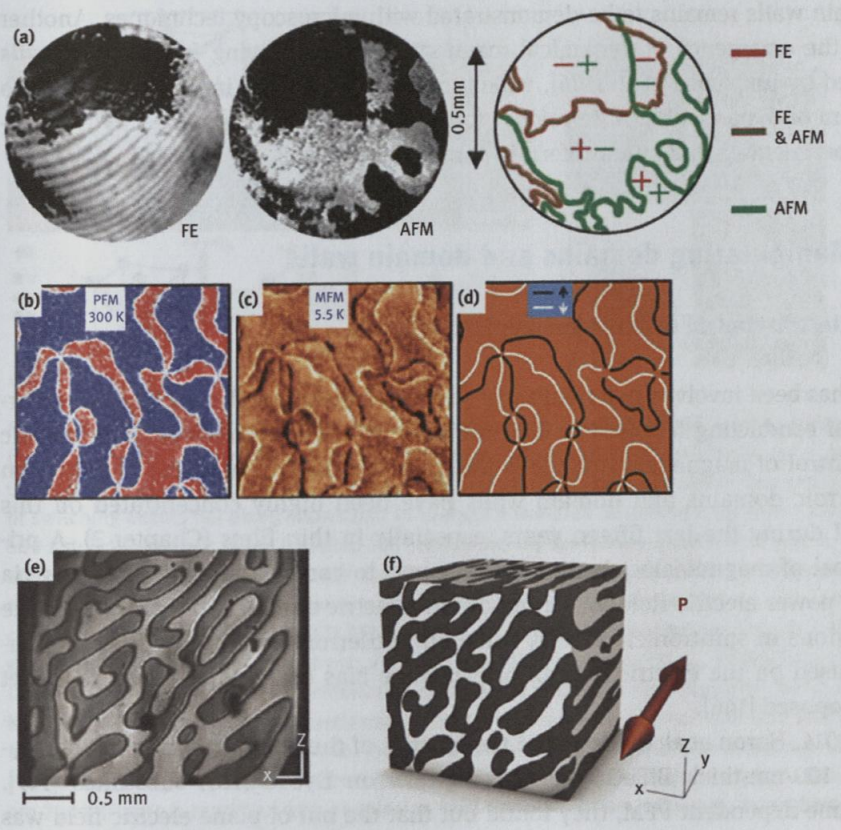

Figure 11.8: Electric and magnetic domains in multiferroics. (a) Coexistence of ferroelectric and antiferromagnetic domains in hexagonal $YMnO_3$ visualized by SHG. Bright and dark areas correspond to regions with different orientations of the order parameter (*P* on the left image – ferroelectric (FE), *L* on the right image – antiferromagnetic (AFM)). The sketch on the right shows that some of the domain walls are both antiferromagnetic and ferroelectric. ((a) is reprinted with permission from Springer Nature, taken from [41]. Copyright 2002 by Springer Nature.) (b) PFM image of hexagonal $ErMnO_3$ showing up- and down-polarized ferroelectric domains. (c) MFM image at low temperature at the same location as in (b) showing an induced magnetic moment at ferroelectric domain walls. (d) Sketch from image in (c), emphasizing the magnetic moments at domain walls of the 16x16 μm^2 image. ((b)–(d) reprinted (adapted) with permission from [140]. Copyright 2012 American Chemical Society.) (e) Multiferroic domain walls in the spin-spiral system $MnWO_4$ visualized by SHG. (f) Illustration showing the 3D distribution of the multiferroic domains in (e). ((e)–(f) reprinted with permission from [37]. Copyright 2009 by the American Physical Society.)

Recently, Farokhipoor et al. reported enhanced magnetism at domain walls in epitaxial thin films of the orthorhombic spin-spiral multiferroic $TbMnO_3$ grown on $SrTiO_3$ [143]. They found out that the macroscopic magnetic signal of the samples is correlated to the density of domain walls of $TbMnO_3$ with different thicknesses. While the results are supported by DFT calculations, direct evidence of magnetism

at domain walls remains to be demonstrated with microscopy techniques. Another idea is the emergence of dynamical magnetic fields at moving ferroelectric walls proposed by Juraschek et al. [144], which extends magnetism in domain walls into the realm of dynamical multiferroicity, foreshadowing exciting perspectives for future experimental work on multiferroic domain walls.

11.3 Manipulating domains and domain walls

11.3.1 Electric control of antiferromagnetic domains

$BiFeO_3$ has been involved in a number of scientific breakthroughs, such as the observation of conducting ferroelectric domain walls [87] and room-temperature electric field control of magnetism [145]. It is thus not surprising that research efforts on multiferroic domains and domain walls have been highly concentrated on this material during the last fifteen years, especially in thin films (Chapter 2). A primary goal of magnetoelectric multiferroics was to control magnetic domains via the low power electric-field switching of ferroelectric domains in view of possible applications in spintronics. $BiFeO_3$ being an antiferromagnetic ferroelectric, concepts based on the electric control of exchange bias of an adjacent ferromagnet were proposed [146].

In 2014, Heron et al. investigated the kinetics of the polarization switching process in 100-nm-thick $BiFeO_3$ thin films grown on $DyScO_3(110)$ substrates [147]. Using time-dependent PFM, they found out that the out-of-plane electric field was giving rise to a 180° reversal of polarization in a two-step switching process combining 71° and 109° switching (Figure 11.9(a)). Ab initio calculations supported these observations with a direct 180° switching having a too high energy barrier compared to the two-step process. In addition, it was predicted that the two-step switching enables an in-plane switching of the canted moment by 180° through the reversal of the rotation of the oxygen octahedra (Figure 11.9(b)). This was experimentally confirmed by visualizing the influence of the ferroelectric switching onto the magnetization of a $Co_{0.9}Fe_{0.1}$ ferromagnet deposited on the film of $BiFeO_3$. Using XMCD-PEEM, the authors observed that, after the application of a 6 V voltage pulse to switch the ferroelectric polarization, the net magnetization of the ferromagnet was reversed (Figure 11.9(c)).

However, these experiments consider that $BiFeO_3$ is in a canted G-type antiferromagnetic phase [148] in contradiction with the measurements of a spin cycloid in low-strained $BiFeO_3$ films grown on substrates such as $DyScO_3(110)$ using Mossbauer and Raman spectroscopies [83]. Using NV magnetometry, Gross et al. recently confirmed that this state was favoured by imaging in real-space the stray field coming from the spin-cycloid of $BiFeO_3$, with an imprint of the ferroelectric stripe-domains onto the magnetic texture (Figure 11.3(h)) [68]. In addition, by defining single ferroelectric

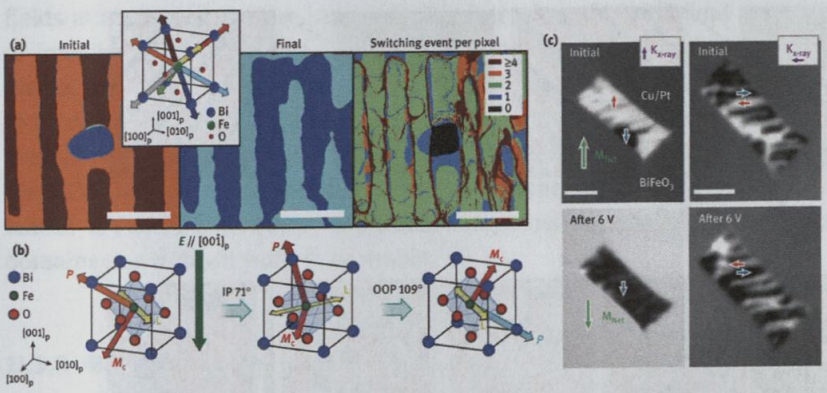

Figure 11.9: Deterministic switching of magnetization with an electric field. (a) Polarization vector images determined from PFM measurements before (initial) and after applying an out-of-plane field (final) to the 100-nm-thick $BiFeO_3$ grown on $SrRuO_3/DyScO_3(110)$. The image on the right (number of switching events per pixel) shows that in average a two-step switching is favored. Scale bars are 500 nm. (b) Schematic of the two-step 180° switching of polarization (P) with a 71° and a subsequent 109° switching. The antiferromagnetic vector (L) and canted moment (M_C) are also represented. Consequently, the two-step switching is accompanied by a 180° rotation of the canted moment of $BiFeO_3$. (c) XMCD-PEEM images of the in-plane moment of a $Co_{0.9}Fe_{0.1}$ layer deposited on $BiFeO_3$ with components viewed perpendicular (vertical $K_{X\text{-}ray}$, where $K_{X\text{-}ray}$ defines the in-plane component of the incident X-ray beam) and parallel to the stripe domains (horizontal $K_{X\text{-}ray}$). The directions of the magnetization in each domain are highlighted with blue and red arrows, which correspond to the local moment direction being perpendicular or parallel to $K_{X\text{-}ray}$. The net $Co_{0.9}Fe_{0.1}$ magnetization (green arrows) reverses after the voltage is applied. Scale bars are 2 μm. (Figure is reprinted with permission from Springer Nature, all panels taken from [147]. Copyright 2014 by Springer Nature.)

domains using the trailing field of the SPM tip, they observed a single spin cycloid within the plane of the film (Figure 11.10(a)). The spin cycloid period is about 70 nm and quantitative NV magnetometry indicates that both the magnetoelectric and the Dzyaloshinskii–Moriya interactions play a role, resulting in a wiggling cycloid (Figure 11.10(b)). Hence, thanks to the magnetoelectric exchange coupling in $BiFeO_3$, the propagation vector of the spin cycloid can be controlled deterministically, envisioning potential applications in the field of magnonics [149] or antiferromagnetic spintronics [150]. In general, the exchange coupling between a strong ferromagnet and a non-collinear antiferromagnetic multiferroic is an intriguing topic that is worth being investigated more thoroughly both theoretically and experimentally.

For large epitaxial strain on $BiFeO_3$, the spin cycloid order is destabilized and a canted G-type antiferromagnetic order emerges [77]. Using SHG, Chauleau et al. observed that two types of submicron antiferromagnetic domains coexist within a single $10 \times 10\ \mu m^2$ ferroelectric domain of $BiFeO_3$ grown on $SrTiO_3(001)$ (Figure 11.3(j)). In addition, they were able to manipulate these antiferromagnetic domains with multiple

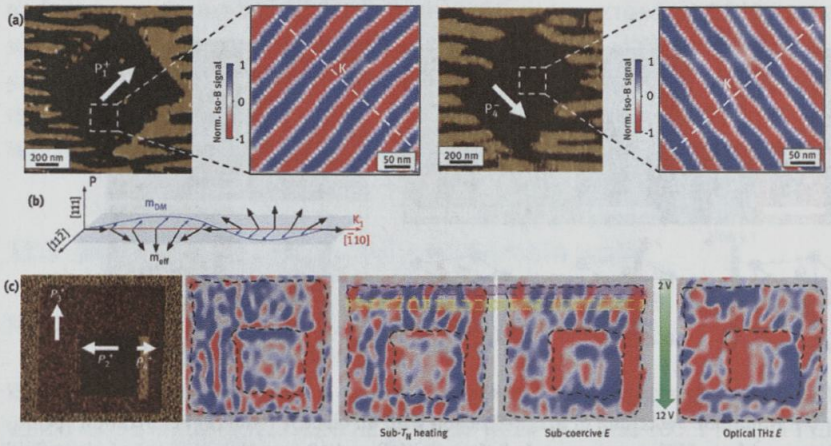

Figure 11.10: Manipulation of the antiferromagnetic order in $BiFeO_3$ thin films. (a) Micron square single domain in $BiFeO_3$ grown on $DyScO_3$(110) read by in-plane PFM and corresponding NV magnetometry image in the center of this square showing the periodic magnetic signal of a spin cycloid. On the right, another micron square single domain with the corresponding magnetic image showing that the propagation vector of the spin cycloid can be rotated by 90° via the magnetoelectric coupling. (b) Sketch of the wiggling cycloid in $BiFeO_3$ with two corresponding canted moments, m_{eff} and m_{DM}, corresponding to magnetoelectric and Dzyaloshinskii–Moriya interactions, respectively. ((a)–(b) are reprinted with permission from Springer Nature, taken from [68]. Copyright 2017 by Springer Nature.) (c) In-plane PFM of a $BiFeO_3$ thin film grown on $SrTiO_3$(001) in which three domains were defined in a $10 \times 10\ \mu m^2$ square. On the right, corresponding SHG images and manipulation with temperature (570 K), electric field (2 to 10 V) and optical THz. ((c) is reprinted with permission from Springer Nature, taken from [69]. Copyright 2017 by Springer Nature.)

stimuli (Figure 11.10(c)). First, manipulating the ferroelectric domains gave rise to a new pattern of antiferromagnetic domains. This is because, due to the magnetoelectric coupling, switching the polarization variants toggles the direction of magnetic anisotropy, which can induce a rotation of the antiferromagnetic vector. Then, they heated the $BiFeO_3$ sample close to the Néel temperature, which led to a reinitialization of the antiferromagnetic domains. They showed that sub-coercive electric fields were also manipulating these antiferromagnetic domains without changing the ferroelectric domain pattern. Finally, 100-fs laser pulses were used to generate a terahertz electrical pulse in the sample. A profound modification of the antiferromagnetic domain pattern resulted, as this matches the range of the antiferromagnetic resonance in $BiFeO_3$. Thus, one can envisage controlling the antiferromagnetic order in a contactless manner using ultrafast light pulses for an all-optical information technology approach.

Another system which is less established than $BiFeO_3$, but which shows significant potential for electric field control of magnetism, is lead zirconium titanate (PZT)-lead iron tantalate (PFT) [151–154]. Using lamellae prepared out of PZT-PFT ceramics, it has been demonstrated that the ferroelectric order switches under applied magnetic

fields at room temperature. An intriguing interplay of electric and magnetic degrees of freedom in PZT-PFT was observed in spatially resolved and integrated measurements, and large coupling constants have been reported [155–158]. The latter is likely to be due to the low structural energy costs of switching between ferroelectric states, evidenced by the relaxor-like domain pattern sometimes observed in thin TEM samples [155] and the small variation in lattice parameters [159]. To evaluate the full potential of PZT-PFT, however, additional comprehensive investigations at the level of domains and domain walls is desirable.

11.3.2 Magnetic control of domain wall charge states in improper ferroelectrics

Spin-driven multiferroics develop domains and domain walls with inseparably entangled electric and magnetic degrees of freedom as introduced in Sections 11.1 and 11.2 (see Chapter 4 for an extended discussion on spin-driven multiferroics). The strong magnetoelectric coupling represents a unique feature of this material class, offering interesting opportunities for the manipulation of domain walls and their electronic properties. The outstanding potential is reflected by proof-of-concept work on iron garnet, where the electrical polarity of domain walls was switched with a magnetic field [160]. In more recent work, a magnetic field was applied to the spin-driven multiferroic $Mn_{0.95}Co_{0.05}WO_4$ to continuously rotate the magnetic easy-plane by 90° and with it the orientation of the ferroelectric polarization (Figure 11.11(a)) [36]. Leo et al. exploited this phenomenon to gain control of the domain wall charge state. They used SHG to image the ferroelectric spin-spiral domains in a $Mn_{0.95}Co_{0.05}WO_4$ single crystal and created neutral 180° ferroelectric domain walls by applying an electric field through macroscopic electrodes (Figure 11.11(b), top). As the primary magnetic order prevents the motion of the wall, a magnetic field of 6 T was used to switch the polarization by 90° without changing the location of the domain wall (Figure 11.11(b), bottom). This way, a magnetic-field-driven change of the charge state was achieved switching from electrically nominally neutral to positively/negatively charged walls [36]. Landau–Lifshitz–Gilbert simulations support the observations of the magnetic-field-induced change of the ferroelectric domain wall charge and give additional insight into the complex Néel-type structure of the domain walls (Figure 11.4(c)).

A similar but discontinuous effect was observed for domain walls in $TbMnO_3$ [39]. In orthorhombic $TbMnO_3$, a spin cycloid appears below $T_C = 27$ K, which breaks inversion symmetry and leads to a spontaneous polarization along the c-axis [50]. Applying a magnetic field along the b-axis alters the orientation of the magnetic easy-plane, giving rise to a polarization flop to the a-axis through a first-order phase transition (Figure 11.11(c)) [50]. Using SHG, Matsubara et al. [39] observed the evolution of multiferroic domains in a $TbMnO_3$ single crystal under the application of an electric field applied along the c-axis. The crystal is naturally forming neutral

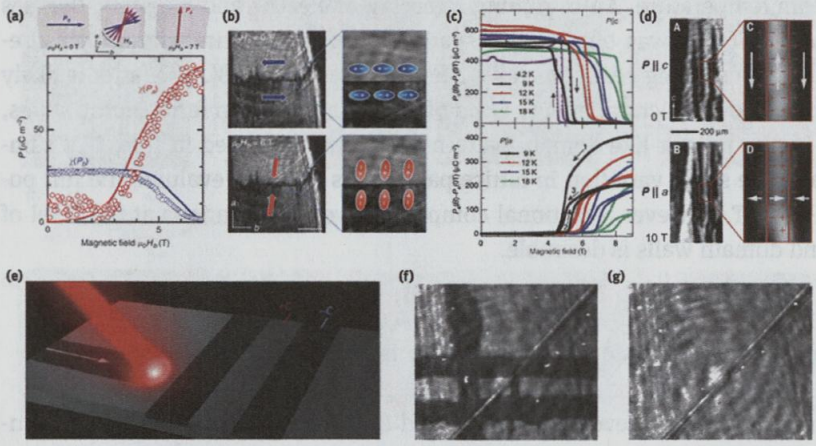

Figure 11.11: Magnetic control of the domain wall charge state in type II multiferroics. (a) Top, sketch illustrating the magnetic-field-induced polarization re-orientation from the b- to the a-axis in $Mn_{0.95}Co_{0.05}WO_4$. Bottom, pyroelectric current (solid lines) and integrated SHG measurements (open symbols) at 5 K, showing the magnetic-field induced rotation of polarization. (b) Top, spatially resolved SHG data of a side-by-side 180° domain wall prepared by applying an electric field along the b-axis at zero magnetic field. Bottom, SHG image of the same area under a magnetic field of 6 T, showing that the wall did not move and becomes a tail-to-tail wall with polarization along the a-axis. The scale bar is 250 μm. ((a) – (b) are reprinted with permission from Springer Nature, taken from [36]. Copyright 2015 by Springer Nature.) (c) Electric polarization flop from the c- to the a-axis in $TbMnO_3$ with a magnetic field applied along the b-axis. ((c) is reprinted with permission from Springer Nature, taken from [50]. Copyright 2003 by Springer Nature.) (d) Domain structure of $TbMnO_3$ across the first-order polarization flop observed with SHG. Top, ferroelectric domain structure in the ground state. Bottom, the application of a magnetic field of 10 T flops the polarization along the a-axis but the domain structure does not change, implying that the walls become charged. ((d) is taken from [39]. Reprinted with permission from AAAS.) (e) Schematic image of the optical poling procedure used by Manz et al. [161] to reversibly write antiferromagnetic domains on $TbMnO_3$. (f) SHG image showing laser-written antiferromagnetic domains with positive (+C, bright) and negative (–C, dark) spin chirality. (g) SHG image of the same region shown in (f) after erasing the laser-written –C domains. ((e) – (g) are reprinted with permission from Springer Nature, taken from [161]. Copyright 2016 by Springer Nature.)

ferroelectric 180° domain walls elongated along the c-axis (Figure 11.9(d), top). As the magnetic exchange interaction is also stronger along the c-axis, both magnetic and electric energies are lowered by the formation of these walls. The team then used SHG at 9 K to track the evolution of domains with polarization parallel to the a- and c-axes under a magnetic field of 10 T applied along the b-axis. Within the resolution of the technique (a few microns), they did not detect any change in the domain pattern from 0 to 10 T while the polarization flopped from the c- to the a-axis (Figure 11.11(d), bottom). This implies that the walls changed from a neutral side-by-side configuration to either tail-to-tail or head-to-head charged states. LLG simulations concluded that the magnetic field along the b-axis exerts an effective

torque on the magnetization around this axis and leads to an identical flop for both up and down polarization previously aligned along the c-axis. The deterministic nature of this multiferroic phase transition allows to convert nominally neutral walls into charged domain walls.

The opportunity to magnetically convert neutral domain walls into charged domain walls is intriguing as it allows, in principle, reversible control of the density of screening charges and, hence, conductivity. This would enable the design of nanosized electrical gates, where ON and OFF states are set by the magnetic field. Going beyond the application of external magnetic (or electric) fields for controlling the domain wall charge state, intense light fields have been used to selectively create nominally neutral and charged walls in spin-driven multiferroics. Manz et al. showed that both nominally neutral and charged walls can be written and erased in $TbMnO_3$ using pulsed- or continuous-wave lasers (Figure 11.11(e)–(g)) [161]. The findings demonstrate the possibility to optically engineer individual domain walls or patterns of higher complexity as required, e.g., for domain-wall-based circuitry. At present, however, any technological merit is clearly suspended by the cryogenic range of the multiferroic phase in spin-spiral multiferroics such as $TbMnO_3$ and $Mn_{0.95}Co_{0.05}WO_4$, and a one-to-one correlation between domain wall charge state and local conductivity is yet to be demonstrated in these materials. Still, the conceptual results reveal completely new pathways for domain wall engineering and highlight the additional functionalities that arise from the strong coupling between electric and magnetic order available in multiferroics.

11.3.3 Tailoring topological states in multiferroics

The ability to electrically write ferroelectric domain patterns with a conductive tip offers exciting possibilities to realize and harness configurations beyond domain walls that will show topological properties (i.e., possessing an integer or semi-integer topological charge Q). The most classical topological textures are vortices ($Q = 1/2$) and skyrmions ($Q = 1$) (antivortices have $Q = -1/2$ and antiskyrmions $Q = -1$) (see also Chapter 9). So far, research has concentrated mostly on topological magnetic structures, but more and more examples of electric textures with non-trivial topology are reported.

After early theoretical predictions by Naumov et al. [162], ferroelectric vortices were first observed in microscale capacitors of PZT by Gruverman et al. in 2008 [163]. Since then, there have been numerous reports in various types of systems (mostly $Pb(Zr,Ti)O_3$, $BaTiO_3$ and $BiFeO_3$). Two main strategies have been pursued, namely: (i) nanostructuration by, e.g., self-organized growth (Figure 12(a)–(c)) [164, 165] or deposition through sacrificial templates [166], and (ii) electric-field manipulation by scanning probe tips [167]. Only in a few of these studies, the topological character of the vortices has been explicitly quantified, for instance, by computing the

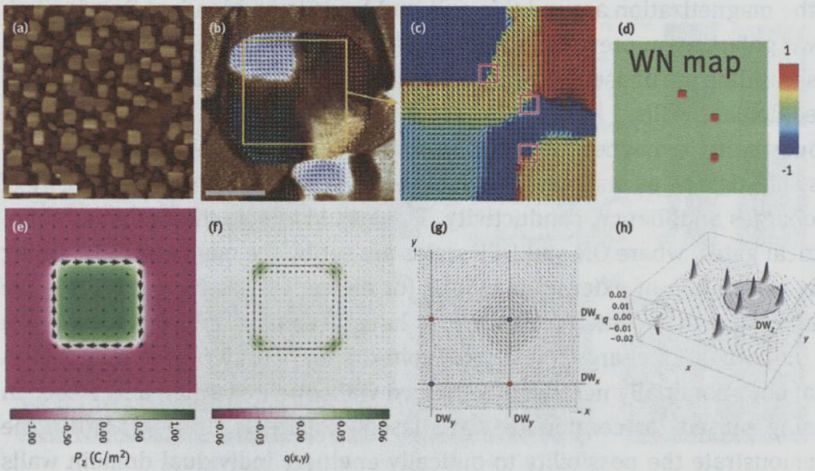

Figure 11.12: Topological structures in multiferroics. (a) Atomic force microscopy image of a $BiFeO_3$ film on $LaAlO_3$ with self-assembled nanoplates. (b) Vector maps of in-plane piezoresponse overlaid on the corresponding out-of-plane PFM contrast of one such nanoplate. (c) In-plane piezoresponse angle maps extracted from the yellow box in (b). (d) Winding number (WN) maps determined from (c). ((a)–(d) are reprinted with permission from Springer Nature, taken from [165]. Copyright 2018 by Springer Nature.) Calculated (e) polarization and (f) Pontryagin density of a nanodomain in $PbTiO_3$ ((e)-(f) reprinted with permission of AAAS from [169] © The Authors, some rights reserved; exclusive licensee American Association for the Advancement of Science. Distributed under a Creative Commons Attribution NonCommercial License 4.0 (CC BY-NC) http://creativecommons.org/licenses/by-nc/4.0/). (g) Vortex structure of a $BaTiO_3$ nanowire embedded in $SrTiO_3$. (h) Associated Pontryagin density map. ((g)–(h) are reprinted with permission from Springer Nature, taken from [168]. Copyright 2015 by Springer Nature.)

vorticity from vector-PFM maps (Figure 11.12(d)) or phase-field simulations mimicking the observed polarization textures. Some works report the electrical manipulation of these vortices, paving the way towards their use in nanoelectronics. Ferroelectric skyrmions were predicted to be stable in nanocomposites (Figure 11.12(g)–(h)) [168] and nanodomains (Figure 11.12(e)–(f)) [169] and, most recently, their existence has been confirmed experimentally in ferroelectric superlattices of $(PbTiO_3)_n/(SrTiO_3)_n$ [170]. To date, whether these ferroelectric topological structures translate into magnetic ones through the local magnetoelectric coupling remains elusive, but new high-sensitivity magnetic microscopy techniques, such as scanning NV microscopy, may shed light on this issue.

In metallic systems with magnetic skyrmion structures, the topological charges can influence the electron transport to produce a topological Hall effect. Many questions arise regarding the consequence of the presence of electric and/or magnetic topological textures in multiferroics in view of their very low conductivity, practically hampering Hall measurements, and more generally on the influence of an electrical topological charge on the macroscopic physical properties. Several papers have

predicted other phenomena arising from the presence of magnetic topological charges, such as the appearance of a topological orbital moment [171, 172] or a spin-chirality-driven inverse Faraday effect [173]. The mounting interest for topological structures in ferroelectrics and multiferroics now calls for similar predictions of exotic effects, driven by electrical topology.

11.4 Conclusions

In this article, we reviewed the recent developments in the field of domains and domain walls in multiferroics. More complete review articles dedicated to domain wall nanoelectronics [55, 56, 174] or functional domain and domain walls in multiferroics [40, 54, 62] can be found elsewhere. Charged domain walls have emerged within the last few years as nanoscale objects with enhanced conductivity or distinct magnetism. They are found naturally in improper ferroelectrics [105] or designed in multiferroics by SPM [114], which opens the way towards reconfigurable nanocircuitry [30, 55] and on-demand spintronic nanocomponents.

New tools are now available to image magnetic textures in antiferromagnets at the local scale. These techniques could help understanding the interplay between ferroelectricity and magnetism in multiferroic domain walls. In addition, the field of antiferromagnetic spintronics [150] could be extended to multifunctional materials, such as multiferroics, in which the propagation of spin waves [175] could be controlled by the electric control of ferroelectric domains.

Finally, the possibility to design topological states [176] with electric-field input is particularly exciting for multiferroics. Theoretical works suggest the possibility to fabricate the electric counterpart of magnetic skyrmions. In addition, recent observations reveal the presence of non-Ising walls in 180° domain walls of regular ferroelectrics ($Pb(Zr,Ti)O_3$ and $LiTaO_3$) [35]. This indicates that complex interconnected chiral electric and magnetic structures could be realized in multiferroics.

References

[1] Schmid H. Multi-ferroic magnetoelectrics. Ferroelectrics. 1994;162:317–38.
[2] Tagantsev AK, Cross LE, Fousek J. Domains in ferroic crystals and thin films. New York: Springer-Verlag, 2010.
[3] Hubert A, Schäfer R. Magnetic domains the analysis of magnetic microstructures. Berlin Heidelberg: Springer-Verlag, 1998.
[4] Tolédano JC, Tolédano P. The landau theory of phase transitions. Singapore: World Scientific, 1987.
[5] Wadhawan VK. Introduction to ferroic materials. Singapore: Gordon and Breach Science Publisher 2, 2000.

[6] Fong DD, Kolpak AM, Eastman JA, Streiffer SK, Fuoss PH, Stephenson GB, et al. Stabilization of monodomain polarization in ultrathin $PbTiO_3$ Films. Phys Rev Lett. 2006;96:127601.
[7] Schilling A, Prosandeev S, McQuaid RG, Bellaiche L, Scott JF, Gregg JM. Shape-induced phase transition of domain patterns in ferroelectric platelets. Phys Rev B Condens Matter Mater Phys. 2011;84:64110.
[8] Schilling A, Byrne D, Catalan G, Webber KG, Genenko YA, Wu GS, et al. Domains in ferroelectric nanodots. Nano Lett. 2009;9:3359–64.
[9] Kalinin S, Gruverman A. Scanning probe microscopy, vol. 2. New York: Springer US, 2007.
[10] Eliseev EA, Fomichv YM, Kalinin SV, Vysochanskii YM, Maksymovich P, Morozovska AN. Labyrinthine domains in ferroelectric nanoparticles: manifestation of a gradient-induced morphological transition. Phys Rev B. 2018;98:54101.
[11] Gilletta F. Evolution of ferroelectric domains in TGS single crystals. Phys Status Solidi. 1972;11:721–7.
[12] Merz WJ. Double hysteresis loop of BaTiO3 at the Curie point. Phys Rev. 1953;91:513–17.
[13] Kittel C. Physical theory of ferromagnetic domains. Rev Mod Phys. 1949;21:541–83.
[14] Kittel C. Theory of the structure of ferromagnetic domains in films and small particles. Phys Rev. 1946;70:965–71.
[15] Frenkel J, Doefman J. Spontaneous and induced magnetisation in ferromagnetic bodies. Nature. 1930;126:274–5.
[16] Mitsui T, Furuichi J. Domain structure of rochelle salt and KH2PO4. Phys Rev. 1953;90:193–202.
[17] Catalan G, Scott JF, Schilling A, Gregg JM. Wall thickness dependence of the scaling law for ferroic stripe domains. J Phys Condens Matter. 2007;19:022201.
[18] Catalan G, Béa H, Fusil S, Bibes M, Paruch P, Barthélémy A, et al. Fractal dimension and size scaling of domains in thin films of multiferroic BiFeO3. Phys Rev Lett. 2008;100:027602.
[19] Scott JF. Nanoferroelectrics: statics and dynamics. J Phys Condens Matter. 2006;18:R361–86.
[20] Kläui M. Head-to-head domain walls in magnetic nanostructures. J Phys Condens Matter. 2008;20:313001.
[21] Eyring EM. Topics in applied physics. Nucl Technol. 1978;39:327–8.
[22] Holtz ME, Shapovalov K, Mundy JA, Chang CS, Yan Z, Bourret E, et al. Topological defects in hexagonal manganites: inner structure and emergent electrostatics. Nano Lett. 2017;17:5883–90.
[23] Choudhury S, Li Y, Odagawa N, Vasudevarao A, Tian L, Capek P, et al. The influence of 180° ferroelectric domain wall width on the threshold field for wall motion. J Appl Phys. 2008;104:84107.
[24] Scott JF, Evans DM, Gregg JM, Gruverman A. Hydrodynamics of domain walls in ferroelectrics and multiferroics: impact on memory devices. Appl Phys Lett. 2016;109:42901.
[25] Tsai F, Khiznichenko V, Cowley JM. High-resolution electron microscopy of 90° ferroelectric domain boundaries in BaTiO3 and Pb(Zr0.52Ti0.48)O3, Ultramicroscopy. 1992;45:55–63.
[26] Dennis MD, Bradt RC. Thickness of 90° ferroelectric domain walls in (Ba,Pb)TiO3 single crystals. J Appl Phys. 1974;45:1931–3.
[27] Lee D, Behera RK, Wu P, Xu H, Sinnott SB, Phillpot SR, et al. Mixed Bloch-Néel-Ising character of 180° ferroelectric domain walls. Phys Rev B. 2009;80:2–5.
[28] Goncalves-Ferreira L, Redfern SA, Artacho E, Salje EK. Ferrielectric twin walls in CaTiO3. Phys Rev Lett. 2008;101:97602.
[29] Tagantsev AK, Courtens E, Arzel L. Prediction of a low-temperature ferroelectric instability in antiphase domain boundaries of strontium titanate. Phys Rev B Condens Matter Mater Phys. 2001;64:2241071–4.
[30] Gregg JM. Exotic domain states in ferroelectrics: searching for vortices and skyrmions. Ferroelectrics. 2012;433:74–87.

[31] Morozovska AN. Domain wall conduction in ferroelectrics. Ferroelectrics. 2012;438:3–19.
[32] Stepkova V, Marton P, Hlinka J. Stress-induced phase transition in ferroelectric domain walls of $BaTiO_3$. J Phys Condens Matter. 2012;24:212201.
[33] De Luca G, Rossell MD, Schaab J, Viart N, Fiebig M, Trassin M. Domain wall architecture in tetragonal ferroelectric thin films. Adv Mater. 2017;29:1605145.
[34] Wei X-K, Jia C-L, Sluka T, Wang B-X, Ye Z-G, Setter N. Néel-like domain walls in ferroelectric $Pb(Zr,Ti)O_3$ single crystals. Nat Commun. 2016;7:12385.
[35] Cherifi-Hertel S, Bulou H, Hertel R, Taupier G, Dorkenoo KD(H), Andreas C, et al. Non-Ising and chiral ferroelectric domain walls revealed by nonlinear optical microscopy. Nat Commun. 2017;8:15768.
[36] Leo N, Bergman A, Cano A, Poudel N, Lorenz B, Fiebig M, et al. Polarization control at spin-driven ferroelectric domain walls. Nat Commun. 2015;6:4–9.
[37] Meier D, Leo N, Maringer D, Lottermoser Th, Fiebig M, Becker P, et al. Topology and manipulation of multiferroic hybrid domains in MnWO4. Phys Rev B. 2009;80:224420.
[38] Domingo N, Farokhipoor S, Santiso J, Noheda B, Catalan G. Domain wall magnetoresistance in BiFeO3 thin films measured by scanning probe microscopy. J Phys Condens Matter. 2017;29:334003.
[39] Matsubara M, Manz S, Mochizuki M, Kubacka T, Iyama A, Aliouane N, et al. Magnetoelectric domain control in multiferroic TbMnO3. Science. 2015;348:1112–15.
[40] Fiebig M, Lottermoser T, Meier D, Trassin M. The evolution of multiferroics. Nat Rev Mater. 2016;1:16046.
[41] Fiebig M, Lottermoser T, Fröhlich D, Goltsev AV, Pisarev RV. Observation of coupled magnetic and electric domains. Nature. 2002;419:818–20.
[42] Redfern SA, Carpenter MA. Transformation processes in mineral. Berlin, Boston: De Gruyter, 2018.
[43] Lines ME, Glass AM. Principles and applications of ferroelectrics and related materials. Oxford: Oxford University Press, 2010.
[44] Salje EK, Carpenter MA. Linear - Quadratic order parameter coupling and multiferroic phase transitions. J Phys Condens Matter. 2011;23:462202.
[45] Salje EK. Phase transitions in ferroelastic and co-elastic crystals. Cambridge University Press, 1991.
[46] Carpenter MA, Salje EK. Elastic anomalies in minerals due to structural phase transitions. Eur J Mineral. 1998;10:693–812.
[47] Fiebig M. Revival of the magnetoelectric effect. J Phys D Appl Phys. 2005;38:R123–R152.
[48] Kimura T. Spiral magnets as magnetoelectrics. Annu Rev Mater Res. 2007;37:387–413.
[49] Mostovoy M. Ferroelectricity in spiral magnets. Phys Rev Lett. 2006;96:67601.
[50] Kimura T, Goto T, Shintani H, Ishizaka K, Arima T, Tokura Y. Magnetic control of ferroelectric polarization. Nature. 2003;426:55–8.
[51] Kagawa F, Mochizuki M, Onose Y, Murakawa H, Kaneko Y, Furukawa N, et al. Dynamics of multiferroic domain wall in spin-cycloidal ferroelectric DyMnO3. Phys Rev Lett. 2009;102:57604.
[52] Lorenz B. Hexagonal manganites—(RMnO 3): class (I) multiferroics with strong coupling of magnetism and ferroelectricity. ISRN Condens Matter Phys. 2013;2013:1–43.
[53] Wu W, Geng Y, Fennie C, Mostovoy M, Cheong S. Visualizing domain wall magnetism and domain magnetoelectricity in multiferroic hexagonal manganites. In: 2015 IEEE International Magnetics Conference (INTERMAG), 2015:1–1.
[54] Meier D. Functional domain walls in multiferroics. J Phys Condens Matter. 2015;27.
[55] Catalan G, Seidel J, Ramesh R, Scott JF. Domain wall nanoelectronics. Rev Mod Phys. 2012;84:119–56.

[56] Bednyakov PS, Sturman BI, Sluka T, Tagantsev AK, Yudin PV. Physics and applications of charged domain walls. npj Comput Mater. 2018;4:65.
[57] Mundy JA, Schaab J, Kumagai Y, Cano A, Stengel M, Krug IP, et al. Functional electronic inversion layers at ferroelectric domain walls. Nat Mater. 2017;16:622.
[58] Sharma P, Zhang Q, Sando D, Lei CH, Liu Y, Li J, et al. Nonvolatile ferroelectric domain wall memory. Sci Adv. 2017;3.
[59] Whyte JR, McQuaid RG, Sharma P, Canalias C, Scott JF, Gruverman A, et al. Ferroelectric domain wall injection. Adv Mater. 2014;26:293–8.
[60] Whyte JR, Gregg JM. A diode for ferroelectric domain-wall motion. Nat Commun. 2015;6:7361.
[61] Bednyakov PS, Sluka T, Tagantsev AK, Damjanovic D, Setter N. Formation of charged ferroelectric domain walls with controlled periodicity. Sci Rep. 2015;5:15819.
[62] Spaldin NA, Ramesh R. Advances in magnetoelectric multiferroics. Nat Mater. 2019;18:203–12.
[63] Dong S, Xiang H, Dagotto E. Magnetoelectricity in multiferroics: a theoretical perspective. Natl Sci Rev. 2019;6:629–41.
[64] Campanini M, Erni R, Rossell MD. Probing local order in multiferroics by transmission electron microscopy. Phys Sci Rev. 2019;0:1–36.
[65] Lahtinen THE, Franke KJA, van Dijken S. Electric-field control of magnetic domain wall motion and local magnetization reversal. Sci Rep. 2012;2:258.
[66] Trassin M, Clarkson JD, Bowden SR, Liu J, Heron JT, Paull RJ, et al. Interfacial coupling in multiferroic/ferromagnet heterostructures. Phys Rev B. 2013;87:134426.
[67] Zhou Z, Trassin M, Gao Y, Gao Y, Qiu D, Ashraf K, et al. Probing electric field control of magnetism using ferromagnetic resonance. Nat Commun. 2015;6:6082.
[68] Gross I, Akhtar W, Garcia V, Martínez LJ, Chouaieb S, Garcia K, et al. Real-space imaging of non-collinear antiferromagnetic order with a single-spin magnetometer. Nature. 2017;549:252–6.
[69] Chauleau JY, Haltz E, Carrétéro C, Fusil S, Viret M. Multi-stimuli manipulation of antiferromagnetic domains assessed by second-harmonic imaging. Nat Mater. 2017;16:803–7.
[70] Merz WJ. The electric and optical behavior of BaTiO3 single-domain crystals. Phys Rev. 1949;76:1221–5.
[71] Forsbergh PW. Domain structures and phase transitions in barium titanate. Phys Rev. 1949;76:1187–201.
[72] Matthias B, von Hippel A. Domain structure and dielectric response of barium titanate single crystals. Phys Rev. 1948;73:1378–84.
[73] Hooton JA, Merz WJ. Etch patterns and ferroelectric domains in BaTiO3 single crystals. Phys Rev. 1955;98:409–13.
[74] Gruverman A, Alexe M, Meier D. Piezoresponse force microscopy and nanoferroic phenomena. Nat Commun. 2019;10:1661.
[75] Rondin L, Tetienne JP, Hingant T, Roch JF, Maletinsky P, Jacques V. Magnetometry with nitrogen-vacancy defects in diamond. Reports Prog Phys. 2014;77:056503.
[76] Lebeugle D, Colson D, Forget A, Viret M, Bataille AM, Gukasov A. Electric-field-induced spin flop in $BiFeO_3$ single crystals at room temperature. Phys Rev Lett. 2008;100:227602.
[77] Sando D, Agbelele A, Rahmedov D, Liu J, Rovillain P, Toulouse C, et al. Crafting the magnonic and spintronic response of BiFeO3 films by epitaxial strain. Nat Mater. 2013;12:641–6.
[78] Sosnowska I, Neumaier TP, Steichele E. Spiral magnetic ordering in bismuth ferrite. J Phys C Solid State Phys. 1982;15:4835–46.
[79] Zhao T, Scholl A, Zavaliche F, Lee K, Barry M, Doran A, et al. Electrical control of antiferromagnetic domains in multiferroic BiFeO3 films at room temperature. Nat Mater. 2006;5:823–9.

[80] Fiebig M, Fröhlich D, Kohn K, Leute St, Lottermoser Th, Pavlov VV, et al. Determination of the magnetic symmetry of hexagonal manganites by second harmonic generation. Phys Rev Lett. 2000;84:5620–3.
[81] Nordlander J, De Luca G, Strkalj N, Fiebig M, Trassin M. Probing ferroic states in oxide thin films using optical second harmonic generation. Appl Sci. 2018;8.
[82] Valencia S, Crassous A, Bocher L, Garcia, V, Moya X, Cherifi RO, et al. Interface-induced room-temperature multiferroicity in BaTiO3. Nat Mater. 2011;10:753.
[83] Seidel J, Maksymovych P, Batra Y, Katan A, Yang SY, He Q, et al. Domain wall conductivity in La-doped BiFeO3. Phys Rev Lett. 2010;105:197603.
[84] Salje EK, Lashley JC. Domain boundary engineering in ferroic and multiferroic materials: a simple introduction. In: Kakeshita T, Fukuda T, Saxena A, Planes A editors, Springer series in materials science. vol. 148 no. 1. Berlin, Heidelberg: Springer Berlin Heidelberg, 2011:1–18.
[85] Scott JF. Room-temperature multiferroic magnetoelectrics. Npg Asia Mater. 2013;5:e72.
[86] Meier D, Maringer M, Lottermoser T, Becker P, Bohatý L, Fiebig M. Observation and coupling of domains in a spin-spiral multiferroic. Phys Rev Lett. 2009;102:107202.
[87] Seidel J, Martin LW, He Q, Zhan Q, Chu YH, Rother A, et al. Conduction at domain walls in oxide multiferroics. Nat Mater. 2009;8:229–34.
[88] Padilla J, Zhong W, Vanderbilt D. First-principles investigation of 180° domain walls in BaTO3. Phys Rev B Condens Matter Mater Phys. 1996;53:R5969–R5973.
[89] McMichael RD, Donahue MJ. Head to head domain wall structures in thin magnetic strips. IEEE Trans Magn. 1997;33, PART 2:4167–9.
[90] Chynoweth AG, Feldmann WL. Ferroelectric domain delineation in triglycine sulphate and domain arrays produced by thermal shocks. J Phys Chem Solids. 1960;15:225–33.
[91] Grekov AA, Adonin AA, Protsenko NP. Encountering domains in sbsi. Ferroelectrics. 1976;13:483–5.
[92] Fesenko EG, Gavrilyatchenko VG, Martinenko MA, Semenchov AF, Lapin IP. Domain structure peculiarities of lead-titanate crystals. Ferroelectrics. 1973;6:61–5.
[93] Surowiak Z, Dec J, Skulski R, Fesenko EG, Gavrilyatchenko VG, Semenchev AF. The domain structure formation at phase transitions. Ferroelectrics. 1978;20:277–9.
[94] Jona F, Shirane G. Ferroelectric crystals, vol, 43. John Wiley & Sons, Ltd, 1963:10–11.
[95] Aristov VV, Kokhanchik LS, Meyer K-P, Blumtritt H. Scanning electron microscopic investigations of peculiarities of the BaTiO3 ferroelectric domain contrast. Phys Status Solidi. 1983;78:229–36.
[96] Aristov VV, Kokhanchik LS, Voronovskii YI. Voltage contrast of ferroelectric domains of lithium niobate in SEM. Phys Status Solidi. 1984;86:133–41.
[97] Sogr AA. Domain structure of ferroelectrics observed in the scanning electron microscope. Ferroelectrics. 1989;97:47–57.
[98] Guyonnet J, Gaponenko I, Gariglio S, Paruch P. Conduction at domain walls in insulating Pb (Zr0.2Ti0.8)O3 thin films. Adv Mater. 2011;23:5377–82.
[99] Tselev A, Yu P, Cao Y, Dedon LR, Martin LW, Kalinin SV, et al. Microwave a.c. conductivity of domain walls in ferroelectric thin films. Nat Commun. 2016;7:11630.
[100] Stolichnov I, Feigl L, McGilly LJ, Sluka T, Wei XK, Colla E, et al. Bent ferroelectric domain walls as reconfigurable metallic–like channels. Nano Lett. 2015;15:8049–55.
[101] Schröder M, Haußmann A, Thiessen A, Soergel E, Woike T, Eng LM. Conducting domain walls in lithium niobate single crystals. Adv Funct Mater. 2012;22:3936–44.
[102] Godau C, Kämpfe T, Thiessen A, Eng LM, Haußmann A. Enhancing the domain wall conductivity in lithium niobate single crystals. ACS Nano. 2017;11:4816–24.

[103] Werner CS, Herr SJ, Buse K, Sturman B, Soergel E, Razzaghi C, et al. Large and accessible conductivity of charged domain walls in lithium niobate. Sci Rep. 2017;7:9862.
[104] Sluka T, Tagantsev AK, Bednyakov P, Setter N. Free-electron gas at charged domain walls in insulating BaTiO3. Nat Commun. 2013;4:1808.
[105] Meier D, Seidel J, Cano A, Delaney K, Kumagai Y, Mostovoy M, et al. Anisotropic conductance at improper ferroelectric domain walls. Nat Mater. 2012;11:284–8.
[106] Choi T, Horibe Y, Yi HT, Choi YJ, Wu W, Cheong SW. Insulating interlocked ferroelectric and structural antiphase domain walls in multiferroic YMnO3. Nat Mater. 2010;9:253–8.
[107] Campbell MP, McConville JP, McQuaid RG, Prabhakaran D, Kumar A, Gregg JM. Hall effect in charged conducting ferroelectric domain walls. Nat Commun. 2016;7:13764.
[108] Schaab J, Skærvø SH, Krohns S, et al. Electrical half-wave rectification at ferroelectric domain walls. Nat Nanotechnol. 2018;13:1028–34.
[109] Schaab J, Krug IP, Nickel F, Dai X, Holtz ME, Cano A, et al. Imaging and characterization of conducting ferroelectric domain walls by photoemission electron microscopy. Appl Phys Lett. 2014;104:232904.
[110] McQuaid RGP, Campbell MP, Whatmore RW, Kumar A, Gregg JM. Injection and controlled motion of conducting domain walls in improper ferroelectric Cu-Cl boracite. Nat Commun. 2017;8:15105.
[111] Oh YS, Luo X, Huang FT, Wang Y, Cheong SW. Experimental demonstration of hybrid improper ferroelectricity and the presence of abundant charged walls in (Ca,Sr)3Ti2O7 crystals. Nat Mater. 2015;14:407–13.
[112] Jiang J, Bai ZL, Chen ZH, He L, Zhang DW, Zhang QH, et al. Temporary formation of highly conducting domain walls for non-destructive read-out of ferroelectric domain-wall resistance switching memories. Nat Mater. 2018;17:49–55.
[113] Jiang AQ, Zhang Y. Next-generation ferroelectric domain-wall memories: principle and architecture. NPG Asia Mater. 2019;11:2.
[114] Crassous A, Sluka T, Tagantsev AK, Setter N. Polarization charge as a reconfigurable quasi-dopant in ferroelectric thin films. Nat Nanotechnol. 2015;10:614–18.
[115] Farokhipoor S, Noheda B. Conduction through 71° domain walls in BiFeO3 thin films. Phys Rev Lett. 2011;107:1–4.
[116] Jungk T, Hoffmann Á, Fiebig M, Soergel E. Electrostatic topology of ferroelectric domains in $YMnO_3$. Appl Phys Lett. 2010;97:012904.
[117] Kumagai Y, Spaldin NA. Structural domain walls in polar hexagonal manganites. Nat Commun. 2013;4:1540.
[118] Småbråten DR, Meier QN, Skjærvø SH, Inzani K, Meier D, Selbach SM. Charged domain walls in improper ferroelectric hexagonal manganites and gallates. Phys Rev Mater. 2018;2:114405.
[119] Wu W, Horibe Y, Lee N, Cheong S-W, Guest JR. Conduction of topologically protected charged ferroelectric domain walls. Phys Rev Lett. 2012;108:77203.
[120] Mosberg AB, Roede ED, Evans DM, Holstad TS, Bourret E, Yan Z, et al. FIB lift-out of conducting ferroelectric domain walls in hexagonal manganites. Appl Phys Lett. 2019;115:122901.
[121] Turner PW, McConville JP, McCartan SJ, Campbell MH, Schaab J, McQuaid RG, et al. Large carrier mobilities in $ErMnO_3$ conducting domain walls revealed by quantitative hall effect measurements. Nano Lett. 2018;18:6381–6.
[122] Schoenherr P, Shapovalov K, Schaab J, Yan Z, Bourret ED, Hentschel M, et al. Observation of uncompensated bound charges at improper ferroelectric Domain Walls. Nano Lett. 2019;19:1659–64.

[123] Skjærvø SH, Småbråten DR, Spaldin NA, Tybell T, Selbach SM. Oxygen vacancies in the bulk and at neutral domain walls in hexagonal YMnO3. Phys Rev B. 2018;98:184102.
[124] Skjærvø SH, Wefring ET, Nesdal SK, Gaukås NH, Olsen GH, Glaum J, et al. Interstitial oxygen as a source of p-type conductivity in hexagonal manganites. Nat Commun. 2016;7:13745.
[125] Wang X, Huang FT, Hu R, Fan F, Cheong SW. Self-poling with oxygen off-stoichiometry in ferroelectric hexagonal manganites. APL Mater. 2015;3:41505.
[126] Selbach SM, Nordli Løvik A, Bergum K, Tolchard JR, Einarsrud M-A, Grande T. Crystal structure, chemical expansion and phase stability of $HoMnO_3$ at high temperature. J Solid State Chem. 2012;196:528–35.
[127] McCarthy GJ, Gallagher PV, Sipe C. Crystal chemistry of catalyst materials. I. Composition and unit cell parameters of $REMnO_3$ phases prepared in air. Mater Res Bull. 1973;8:1277–84.
[128] Griffin SM, Reidulff M, Selbach SM, Spaldin NA. Defect chemistry as a crystal structure design parameter: intrinsic point defects and Ga substitution in $InMnO_3$. Chem Mater. 2017;29:2425–34.
[129] Holstad TS, Evans DM, Ruff A, Småbråten DR, Schaab J, Tzschaschel Ch, et al. Electronic bulk and domain wall properties in B -site doped hexagonal ErMnO3. Phys Rev B. 2018;97:85143.
[130] Hassanpour E, Wegmayr V, Schaab J, Yan Z, Bourret E, Lottermoser Th, et al. Robustness of magnetic and electric domains against charge carrier doping in multiferroic hexagonal $ErMnO_3$. New J Phys. 2016;18:43015.
[131] Meier QN, Lilienblum M, Griffin SM, Conder K, Pomjakushina E, Yan Z, et al. Global formation of topological defects in the multiferroic hexagonal manganites. Phys Rev X. 2017;7:41014.
[132] Griffin SM, Lilienblum M, Delaney KT, Kumagai Y, Fiebig M, Spaldin NA. Scaling behavior and beyond equilibrium in the hexagonal manganites. Phys Rev X. 2012;2:41022.
[133] Griffin SM, Spaldin NA. On the relationship between topological and geometric defects. J Phys Condens Matter. 2017;29:343001.
[134] Balke N, Choudhury S, Jesse S, Huijben M, Chu YH, Baddorf AP, et al. Deterministic control of ferroelastic switching in multiferroic materials. Nat Nanotechnol. 2009;4:868–75.
[135] Lubk A, Gemming S, Spaldin NA. First-principles study of ferroelectric domain walls in multiferroic bismuth ferrite. Phys Rev B. 2009;80:104110.
[136] Daraktchiev M, Catalan G, Scott JF. Landau theory of domain wall magnetoelectricity. Phys Rev B. 2010;81:224118.
[137] Scheinfein MR, Unguris J, Kelley MH, Pierce DT, Celotta RJ. Scanning electron microscopy with polarization analysis (SEMPA). Rev Sci Instrum. 1990;61:2501–27.
[138] Zhang JX, Zeches RJ, He Q, Chu YH, Ramesh R. Nanoscale phase boundaries: a new twist to novel functionalities. Nanoscale. 2012;4:6196–204.
[139] He Q, Yeh CH, Yang JC, Singh-Bhalla G, Liang CW, Chiu PW, et al. Magnetotransport at domain walls in BiFeO3. Phys Rev Lett. 2012;108:1–5.
[140] Geng Y, Lee N, Choi YJ, Cheong SW, Wu W. Collective magnetism at multiferroic vortex domain walls. Nano Lett. 2012;12:6055–9.
[141] Meier D, Ryll H, Kiefer K, Klemke B, Hoffmann JU, Ramesh R, et al. Mutual induction of magnetic 3d and 4f order in multiferroic hexagonal ErMnO3. Phys Rev B. 2012;86:184415.
[142] Taniguchi K, Abe N, Takenobu T, Iwasa Y, Arima T. Ferroelectric polarization flop in a frustrated magnet MnWO4 induced by a magnetic field. Phys Rev Lett. 2006;97:097203.
[143] Farokhipoor S, Magén C, Venkatesan S, Íñiguez J, Daumont CJ, Rubi D, et al. Artificial chemical and magnetic structure at the domain walls of an epitaxial oxide. Nature. 2014;515:379–83.
[144] Juraschek DM, Fechner M, Balatsky AV, Spaldin NA. Dynamical multiferroicity. Phys Rev Mater. 2017;1:14401.

[145] Heron JT, Trassin M, Ashraf K, Gajek M, He Q, Yang SY, et al. Electric-field-induced magnetization reversal in a ferromagnet-multiferroic heterostructure. Phys Rev Lett. 2011;107:217202.
[146] Bibes M, Barthélémy A. Multiferroics: towards a magnetoelectric memory. Nat Mater. 2008;7:425–6.
[147] Heron JT, Bosse JL, He Q, Gao Y, Trassin M, Ye L, et al. Deterministic switching of ferromagnetism at room temperature using an electric field. Nature. 2014;516:370–3.
[148] Ederer C, Spaldin NA. Influence of strain and oxygen vacancies on the magnetoelectric properties of multiferroic bismuth ferrite. Phy Rev B. 2005;71:224103.
[149] Rovillain P, de Sousa R, Gallais Y, Sacuto A, Méasson MA, Colson D, et al. Electric-field control of spin waves at room temperature in multiferroic BiFeO3. Nat Mater. 2010;9:975–9.
[150] Jungwirth T, Marti X, Wadley P, Wunderlich J. Antiferromagnetic spintronics. Nat Nanotechnol. 2016;11:231–41.
[151] Scott JF, Evans DM, Katiyar RS, McQuaid RG, Gregg JM. Nonequilibrium ferroelectric-ferroelastic 10 nm nanodomains: wrinkles, period-doubling, and power-law relaxation. J Phys Condens Matter. 2017;29:304001.
[152] Glinchuk MD, Eliseev EA, Morozovska AN. Novel room temperature multiferroics on the base of single-phase nanostructured perovskites. J Appl Phys. 2014;116:54101.
[153] Glinchuk MD, Eliseev EA, Morozovska AN. Landau-Ginzburg description of anomalous properties of novel room temperature multiferroics Pb(Fe1/2Ta1/2)x(Zr0.53Ti0.47)1-xO3 and Pb(Fe1/2Nb1/2)x(Zr0.53Ti0.47)1-xO3. J Appl Phys. 2016;119:24102.
[154] Wu Y-C, Ho SZ, Liu YC, Liou Y-D, Liu W-Y, Huang S-W, et al. Room temperature multiferroic PZTFT thin films. ACS Appl Electron Mater, 2019.
[155] Evans DM, Schilling A, Kumar A, Sanchez D, Ortega N, Arredondo M, et al. Magnetic switching of ferroelectric domains at room temperature in multiferroic PZTFT. Nat Commun. 2013;4:1534.
[156] Evans DM, Schilling A, Kumar A, Sanchez D, Ortega N, Katiyar RS, et al. Switching ferroelectric domain configurations using both electric and magnetic fields in Pb(Zr,Ti)O_3-Pb(Fe,Ta)O_3 single-crystal lamellae. Philos Trans R Soc A. 2014;372:20120450.
[157] Schiemer J, Carpenter MA, Evans DM, Gregg, JM, Schilling A, Arredondo M, et al. Studies of the room-temperature multiferroic Pb(Fe0.5Ta0.5)0.4(Zr0.53Ti0.47)0.6O3: resonant ultrasound spectroscopy, dielectric, and magnetic phenomena. Adv Funct Mater. 2014;24:2993–3002.
[158] Evans DM, Alexe M, Schilling A, Kumar A, Sanchez D, Ortega N, et al. The Nature of magnetoelectric coupling in Pb(Zr,Ti)O3-Pb(Fe,Ta)O3. Adv Mater. 2015;27:6068–73.
[159] Sanchez DA, Ortega N, Kumar A, Roque-Malherbe R, Polanco R, Scott JF, et al. Symmetries and multiferroic properties of novel room-temperature magnetoelectrics: lead iron tantalate – lead zirconate titanate (PFT/PZT). AIP Adv. 2011;1:42169.
[160] Pyatakov AP, Sechin DA, Sergeev AS, Nikolaev AV, Nikolaeva EP, Logginov AS, et al. Magnetically switched electric polarity of domain walls in iron garnet films. Epl. 2011;93:17001.
[161] Manz S, Matsubara M, Lottermoser T, Büchi J, Iyama A, Kimura T, et al. Reversible optical switching of antiferromagnetism in TbMnO3. Nat Photonics. 2016;10:653–6.
[162] Naumov II, Bellaiche L, Fu H. Unusual phase transitions in ferroelectric nanodisks and nanorods. Nature. 2004;432:737–40.
[163] Gruverman A, Wu D, Fan HJ, Vrejoiu I, Alexe M, Harrison RJ, et al. Vortex ferroelectric domains. J Phys Condens Matter. 2008;20:342201.

[164] Ma J, Ma J, Zhang Q, Peng R, Wang J, Liu C, et al. Controllable conductive readout in self-assembled, topologically confined ferroelectric domain walls. Nat Nanotechnol. 2018;13:947–52.
[165] Kim KE, Jeong S, Chu K, Lee JH, Kim GY, Xue F, et al. Configurable topological textures in strain graded ferroelectric nanoplates. Nat Commun. 2018;9:1–12.
[166] Li Z, Wang Y, Tain G. High-density array of ferroelectric nanodots with robust and reversibly switchable topological domain states. Sci Adv. 2017;3:e1700919.
[167] Balke N, Winchester B, Ren W, Chu, YH, Morozovska AN, Eliseev EA, et al. Enhanced electric conductivity at ferroelectric vortex cores in BiFeO3. Nat Phys. 2012;8:81–8.
[168] Nahas Y, Prokhorenko S, Louis L, Gui Z, Kornev I, Bellaiche L. Discovery of stable skyrmionic state in ferroelectric nanocomposites. Nat Commun. 2015;6:1–6.
[169] Gonçalves MA, Escorihuela-Sayalero C, Garca-Fernández P, Junquera J, Íñiguez J. Theoretical guidelines to create and tune electric skyrmion bubbles. Sci Adv. 2019;5:eaau7023.
[170] Das S, Tang YL, Hong Z, GonÇalves MA, McCarter MR, Klewe C, et al. Observation of room-temperature polar skyrmions. Nature. 2019;568:368–72.
[171] Hoffmann M, Weischenberg J, Dupé B, Freimuth F, Ferriani P, Mokrousov Y, et al. Topological orbital magnetization and emergent Hall effect of an atomic-scale spin lattice at a surface. Phys Rev B. 2015;92:020401.
[172] Hanke J, Freimuth F, Blügel S, Mokrousov Y. Prototypical topological orbital ferromagnet γ-FeMn. Sci Rep. 2017;7:41078.
[173] Taguchi K, Tatara G. Inverse faraday effect driven by spin chirality in weak ferromagnets. J Korean Phys Soc. 2013;62:1759–62.
[174] Vasudevan RK, Wu W, Guest JR, Baddorf AP, Morozovska AN, Eliseev EA, et al. Domain wall conduction and polarization-mediated transport in ferroelectrics. Adv Funct Mater. 2013;23:2592–616.
[175] Lebrun R, Ross A, Bender SA, Qaiumzadeh A, Baldrati L, Cramer J, et al. Tunable long-distance spin transport in a crystalline antiferromagnetic iron oxide. Nature. 2018;561:222–5.
[176] Huang F-T, Cheong S-W. Aperiodic topological order in the domain configurations of functional materials. Nat Rev Mater. 2017;2:17004.